

The Onset of Depletion-Induced Seismicity in Slip-Weakening Faults With Interacting Peaked Shear Stresses

Uenishi and Rice Extended

Jansen, J. D.; Meulenbroek, B. J.

DOI

10.1029/2025JB031577

Publication date

Document Version Final published version

Published in

Journal of Geophysical Research: Solid Earth

Citation (APA)

Jansen, J. D., & Meulenbroek, B. J. (2025). The Onset of Depletion-Induced Seismicity in Slip-Weakening Faults With Interacting Peaked Shear Stresses: Uenishi and Rice Extended. Journal of Geophysical Research: Solid Earth, 130(10), Article e2025JB031577. https://doi.org/10.1029/2025JB031577

Important note

To cite this publication, please use the final published version (if applicable). Please check the document version above.

Copyright

Other than for strictly personal use, it is not permitted to download, forward or distribute the text or part of it, without the consent of the author(s) and/or copyright holder(s), unless the work is under an open content license such as Creative Commons.

Please contact us and provide details if you believe this document breaches copyrights. We will remove access to the work immediately and investigate your claim.



JGR Solid Earth

-

RESEARCH ARTICLE

10.1029/2025JB031577

Key Points:

- We derived an expression for the nucleation length in a slip-weakening fault loaded with a coupled doublepeaked shear stress distribution
- This criterion is especially relevant for depletion-induced fault slip in reservoirs with displaced faults with large offsets
- It yields a code-independent termination criterion for numerical simulation of depletion-induced aseismic slip and the onset of seismicity

Supporting Information:

Supporting Information may be found in the online version of this article.

Correspondence to:

J. D. Jansen, j.d.jansen@tudelft.nl

Citation:

Jansen, J. D., & Meulenbroek, B. J. (2025). The onset of depletion-induced seismicity in slip-weakening faults with interacting peaked shear stresses: Uenishi and Rice extended. *Journal of Geophysical Research: Solid Earth, 130*, e2025JB031577. https://doi.org/10.1029/2025JB031577

Received 14 MAR 2025 Accepted 16 SEP 2025

Author Contributions:

Conceptualization: J. D. Jansen.

B. J. Meulenbroek
Formal analysis: B. J. Meulenbroek
Funding acquisition: J. D. Jansen
Investigation: J. D. Jansen,
B. J. Meulenbroek
Methodology: J. D. Jansen,
B. J. Meulenbroek
Software: J. D. Jansen
Validation: J. D. Jansen
Visualization: J. D. Jansen
Writing – original draft: J. D. Jansen,
B. J. Meulenbroek

© 2025. The Author(s).

This is an open access article under the terms of the Creative Commons

Attribution License, which permits use, distribution and reproduction in any medium, provided the original work is properly cited.

The Onset of Depletion-Induced Seismicity in Slip-Weakening Faults With Interacting Peaked Shear Stresses: Uenishi and Rice Extended

J. D. Jansen¹ and B. J. Meulenbroek²

¹Department of Geoscience and Engineering, Delft University of Technology, Delft, The Netherlands, ²Delft Institute of Applied Mathematics, Delft University of Technology, Delft, The Netherlands

Abstract Depletion-induced fault slip and seismicity in the Groningen natural gas field are known to be caused by compaction of reservoir rock, most likely at locations in faults where reservoir rock juxtaposes nonreservoir rock leading to severely-peaked shear stresses at the reservoir-fault corners. The resulting fault slip is probably initially aseismic until a critical nucleation length is reached. Under the assumption of slip-weakening friction, the nucleation length can be approximated with a classic stability criterion developed by Uenishi and Rice (U&R) in 2003 for a single-peaked stress distribution. Earlier work revealed that the validity of this criterion breaks down when the fault offset exceeds approximately 70% of the reservoir height because interaction effects between neighboring stress peaks can no longer be ignored. We therefore extended the U&R criterion to cope with such a double-peaked shear stress. The key mathematical innovation involves a singular functional form of the slip gradient which allows for the formulation of slip-patch end conditions that can be directly extended to multiple patches. We derived an exact double-patch eigenvalue criterion and an approximate closed-form "Extended Uenishi and Rice (EU&R) criterion" that is dependent on a parameter representing the scaled distance between the slip patches. For examples with parameter values roughly based on those of the Groningen field, we found a good agreement between our approximate EU&R criterion and an exact eigenvalue-based approach. Our results can serve as a robust code-independent termination criterion during numerical simulation of depletioninduced onset of seismicity resulting from natural gas or geothermal energy production.

Plain Language Summary Production of natural gas from a subsurface reservoir (porous rock) leads to a decrease in pressure and a shrinkage of the rock. Reservoirs often contain faults: near-vertical jumps in the rock layers. In these, the shrinking porous rock may be located opposite non-shrinking rock leading to stress build-up and fault slip. Slip in itself is not a problem if it occurs gradually (aseismically). However, slip may also lead to a reduction in the rock friction, and when the slipping area (slip patch) becomes too large and the reduction in friction too much, the configuration may become unstable leading to a sudden release of built-up stresses (an earthquake). In 2003, Uenishi and Rice (U&R) developed an expression that predicts when instability occurs for a single patch. However, when the fault has been displaced over a large height, the stresses may originate from two close-by located patches such that an earthquake may occur earlier than expected. Our paper presents an "Extended U&R criterion" that does take the influence between the patches into account. This may be of help in computer simulations of natural gas or geothermal energy production to better understand the cause of earthquakes and possibly contribute to preventing them.

1. Introduction

1.1. Motivation

The motivation for our paper stems from the occurrence of earthquakes in the huge Groningen natural gas field in the Netherlands, an area where no natural seismicity was ever observed, or recorded in historic documents, before the start of gas production. The earthquakes only started after decades of reservoir pressure depletion, and occur until today, even though the field has recently been closed. Their location has been identified as inside or just above the reservoir at three km depth. Even though they are of a much smaller magnitude than the heaviest natural and injection-triggered earthquakes, they are strongly felt because of their relatively shallow origin, the low soil stiffness near the surface, and the high population density (Bourne et al., 2018; Van Thienen-Visser & Breunese, 2015). Serious social unrest ultimately led to an early closure of the field. Understandably, there are major

21699356, 2025, 10, Downloaded from https://agupubs

onlinelibrary.wiley.com/doi/10.1029/2025JB031577 by Technical University Delft, Wiley Online Library on [30/10/2025].

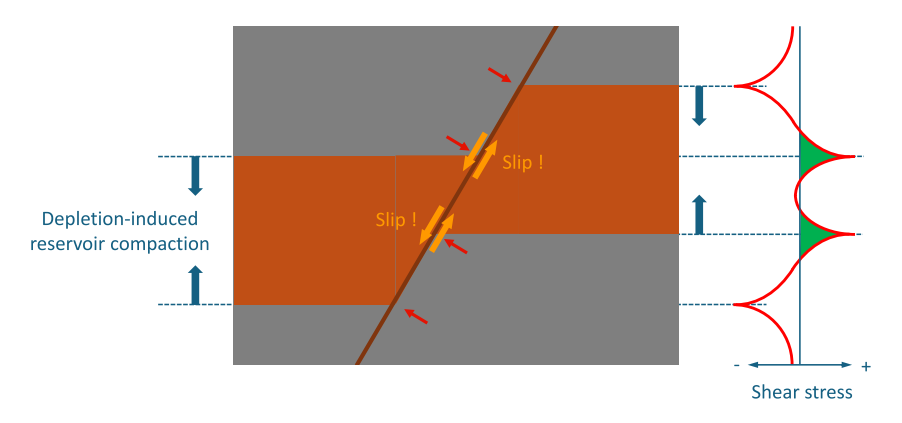


Figure 1. Internal forcing due to compaction as a result of depletion or cooling in a reservoir with a (non-sealing) displaced fault (after Van den Bogert (2015)). Severe "pre-slip Coulomb stress" concentrations (proportional to shear stress concentrations) develop at the reservoir-fault corners. Positive pre-slip Coulomb stresses (green areas) result in fault slip.

concerns that emerging subsurface applications for the energy transition may cause similar unexpected earth-quakes in currently seismically silent areas (Pluymakers et al., 2023).

1.2. Depletion-Induced Seismicity

There are strong indications that depletion-induced seismicity in the Groningen field, and similar reservoirs in the North of the Netherlands and Germany, develops through an internal forcing mechanism: pressure depletion leads to sharply peaked shear stresses at the reservoir/fault corners in bounding or intra-reservoir displaced normal faults, that is, in faults where reservoir rock juxtaposes non-reservoir rock. Fault slip develops in these highly stressed regions, most likely initially aseismically but possibly resulting in earthquakes at a later stage. This mechanism has been described, to various levels of detail, in early studies (Mulders, 2003; Nagelhout & Roest, 1997; Roest & Kuilman, 1994), more recent numerical simulations (Buijze et al., 2017, 2019; Candela et al., 2019; Orlic & Wassing, 2013; Van den Bogert, 2015, 2018; Van den Bogert & Eijs, 2020; Van Wees et al., 2017; Zbinden et al., 2017) and recent semi-analytical work (Cornelissen et al., 2024; Jansen et al., 2019; Jansen & Meulenbroek, 2022; Wu et al., 2021). A similar mechanism due to injection in reservoirs with displaced faults has also been described; see, for example, studies into subsurface CO₂ storage by Cappa and Rutqv-ist (2011); Rutqvist et al. (2016), while thermal stresses may cause similar effects (Buijze et al., 2023; Marelis et al., 2024; Van den Hoek & Poessé, 2021).

1.3. Peaked Shear Stresses

The peculiar effect of displaced normal faults is that they result in peaked shear stress distributions at distinct locations resulting in slip patches that grow in size in a predictable direction with increasing depletion or injection; see Figure 1. In the Groningen field, many of such displaced faults are present. In fact, from the more than 1,100 faults that have been mapped, the vast majority are displaced (normal) faults, many of which have a significant offset; see Figure 2. We note that induced stresses just above or below the reservoir may also influence seismicity in the Groningen field (Dempsey & Suckale, 2023; Smith et al., 2022), while the same holds for stiffness contrasts between reservoir and over/underburden and the presence of a thick layer of visco-elastic salt above the reservoir (Orlic & Wassing, 2013). However, in any case, displaced faults are likely to play an important role, and in this paper we therefore focus on the onset of seismicity in reservoirs intersected by such faults.

As illustrated in Figure 1, a typical characteristic of the internal forcing mechanism is the development of a preslip Coulomb stress distribution (which is proportional to the shear shear stress distribution) along the displaced fault, with four stress peaks of which two are positive-valued, and two negative-valued. (In case of a bounding fault, or a sealing fault experiencing strong differential pressure, only two peaks will develop; a positive and a negative one). In case of four peaks, their locations coincide with the internal and external reservoir-fault corners, and their signs depend on whether the reservoir experiences a pressure increase (positive peaks at the outer corners) or decrease (positive at the inner corners, as in Figure 1). The precise shape and magnitude of the peaks depend on the fault geometry, the material properties and the pressure and temperature distributions in the surrounding rock, and may be smoothed by mechanisms such as rock plasticity or pressure diffusion. However, the

21699356, 2025, 10, Downloaded from https://agupubs.onlinelibrary.wiley.com/doi/10.1029/2025JB031577 by Technical University Delft,

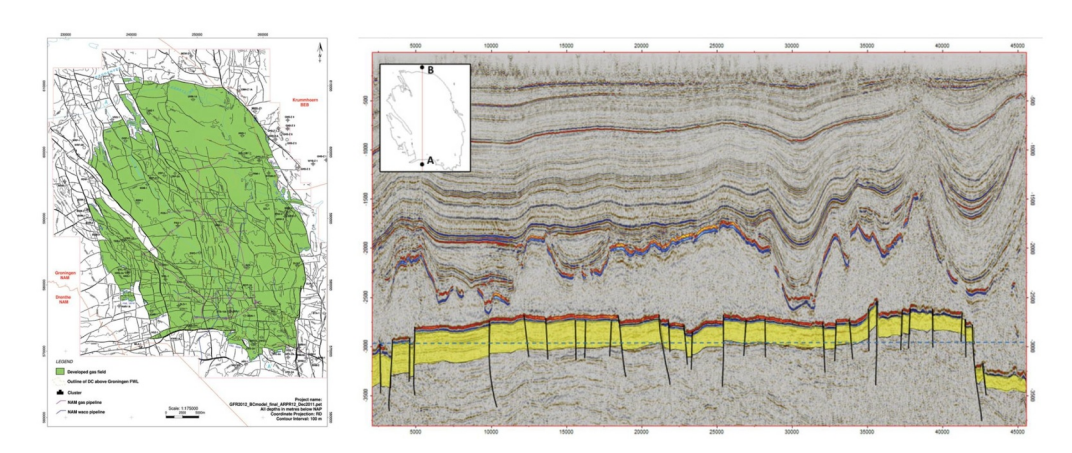


Figure 2. Left: Structural map of the Groningen gas field. Right: North-South cross-section through the field. The reservoir, represented in yellow, is intersected by numerous faults, many of which have a significant offset. Figures taken from De Jager and Visser (2017).

four-peaked Coulomb stress distribution remains a characteristic feature of displaced faults in a reservoir experiencing injection or depletion.

1.4. Slip Weakening and Interacting Stress Peaks

The positive stress peaks may result in two patches of local fault slip, which will grow toward each other in case of a depleting reservoir and away from each other in case of an injection scenario (Jansen et al., 2019). Typically, the slip will initially be aseismic, but in both situations a critical pressure may be reached, the nucleation pressure, at which the fault becomes unstable and a seismic event occurs (Buijze et al., 2017, 2019; Jansen & Meulenbroek, 2022; Van den Bogert, 2018). A prerequisite for instability is some form of loss of fault strength with increasing slip or slip velocity, and the two dominant corresponding physical models are slip-weakening friction, and rate-and-state friction with velocity weakening (Ohnaka, 2013; Scholz, 2019). Characteristic values of fault friction for various lithologies in the Groningen field have been determined by Hunfeld et al. (2017).

In 2003, Uenishi and Rice presented a seminal stability analysis for a fault loaded with a constant (effective) normal stress and a single-peaked shear stress distribution, in combination with slip-weakening fault strength (Uenishi & Rice, 2003). Building on an earlier result by Dascalu et al. (2000), they formulated an eigen value problem and derived a remarkably simple expression for the critical slip patch length, known as the nucleation length in terms of elastic properties of the rock and the slope of the fault strength reduction during slip. Moreover, they demonstrated that this nucleation length is universal, in the sense that it doesn't depend on the exact form of the peaked stress distribution.

Unlike in Uenishi and Rice's analysis, the (effective) normal stress in the displaced fault configuration that we address is not constant, while, moreover, the shear stresses in the two slip patches may influence each other. Jansen and Meulenbroek (2022) made an attempt to analyze these complicating aspects with a semi-analytical approach using classical techniques from dislocation-based fracture mechanics. They demonstrated that the non-constant normal stresses have only a minor effect on the nucleation length, and could numerically show that interaction becomes relevant for faults with a vertical displacement (fault throw) larger than about 70% of the reservoir height. In the paper by Jansen and Meulenbroek (2022), the interaction effect was approximately accounted for with an iterative approach, which, however, cannot be shown to converge and does not allow the formulation of an eigenvalue problem as required to obtain an expression for the nucleation length.

Meulenbroek and Jansen (2024) further analyzed this problem and developed a mathematically more rigorous and computationally efficient approach to describe fault slip in case of interaction between slip patches with constant friction. However, this approach is less suitable to describe interaction with slip-weakening friction, while, moreover, it still cannot be used to obtain an eigenvalue-based solution for the nucleation length. In the present paper we introduce a different semi-analytical approach that does allow to do so, and we investigate the effects of slip-weakening friction and coupled stress peaks on fault stability and the corresponding nucleation length and nucleation pressure.

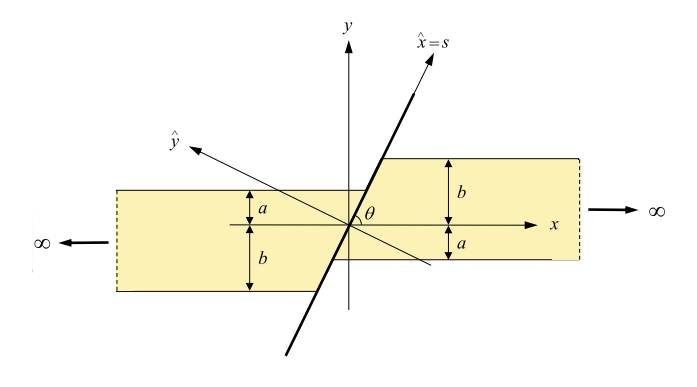


Figure 3. Infinitely wide reservoir with a displaced normal fault (Jansen & Meulenbroek, 2022).

2. Problem Definition

2.1. Induced Fault Stresses

We start from a simple two-dimensional plane-strain reservoir model with a single displaced and inclined fault, which we also used in earlier publications; see Figure 3. We assume the reservoir to be either of finite width or infinitely wide and of height h=a+b, intersected by a displaced non-sealing zero-width fault with an offset of magnitude $t_f=b-a$ and a dip angle θ . As described above, depletion typically results in the development of two slip patches starting from the "internal" reservoir-fault corners at $y=\pm a$; see Figure 4 which displays results for an example from Meulenbroek and Jansen (2024). The corresponding parameter values are listed in Table 1 and are roughly based on those of the Groningen field. The stresses in this example were computed from analytical expressions given in Appendix A, but similar

result may be obtained with numerical simulation (Buijze et al., 2017, 2019; Novikov et al., 2024; Van den Bogert, 2015, 2018; Van Wees et al., 2017, 2019).

Slip-provoking conditions in the fault occur in locations where

$$|\tau| > \tau_{sl} = \kappa - \mu \sigma', \quad \kappa \ge 0, \quad \sigma' < 0,$$
 (1)

where τ is the shear stress in the fault, τ_{sl} the slip stress, κ cohesion, σ' the effective normal stress, and μ the friction coefficient. Note that we use the solid mechanics sign convention in which negative normal stresses correspond to compression. The (negative) effective normal stress is then defined as

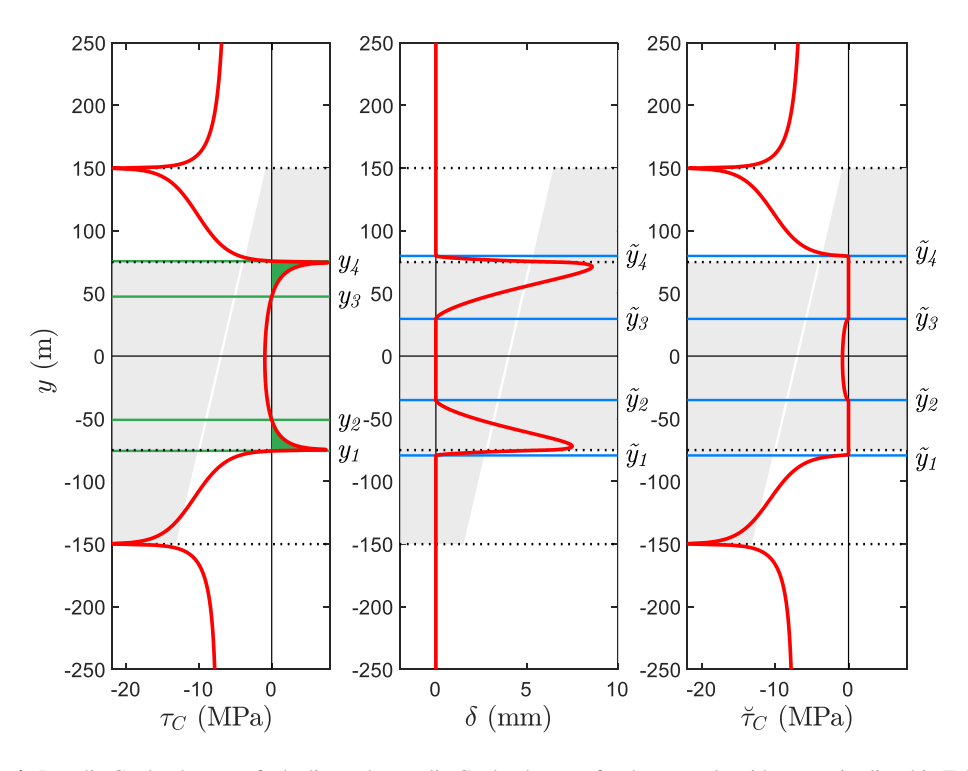


Figure 4. Pre-slip Coulomb stress, fault slip, and post-slip Coulomb stress for the example with properties listed in Table 1 (small-offset case; constant friction with $\mu_{st}=0.52$). Left: pre-slip Coulomb stress $\tau_C=\tau-\tau_{st}$. Middle: fault slip δ . Right: post-slip Coulomb stress $\tilde{\tau}_C=\tau_C+\tilde{\tau}$. The green horizontal lines at y=-76, -51, 47, and 76m in the left figure correspond to the zeros $y_i, i=1,\ldots,4$, of the pre-slip Coulomb stress. The blue horizontal lines at y=-80, -33, 29, and 80m in the right figure correspond to the slip patch boundaries \tilde{y}_i which are also the zeros of the post-slip Coulomb stress. The horizontal black dotted lines in both figures represent the four coordinate values y=-a,-b,b and a which correspond to the top and bottom of the reservoir blocks, indicated in gray, at each side of the fault.

Table 1
Parameter Values for the Examples (Jansen & Meulenbroek, 2022)

Symbol	Property	Value	SI units
a	Small-offset case	75	m
b	"	150	m
а	Large-offset case	190	m
b	"	35	m
D_0	Depth at reservoir center $(y = 0)$	3,500	m
g	Acceleration of gravity	9.81	m/s ²
G	Shear modulus	6,500	MPa
K^0	Ratio of initial effective horizontal to vertical stresses	0.5	_
Δp	Incremental reservoir pressure	-25	MPa
p_0^0	Initial reservoir pressure at reservoir center	35	MPa
α	Biot coefficient	0.9	_
β	Effective stress coefficient for fault friction	0.9	_
δ_c	Cut-off slip distance in slip-weakening law	0.02	m
η	Regularization parameter	0.10	m
θ	Dip angle	70	deg.
κ	Cohesion	0	MPa
μ_{dyn}	Dynamic friction coefficient	0.30	_
μ_{st}	Static friction coefficient	0.52	_
ν	Poisson's coefficient	0.15	_
$ \rho_{jl} $	Fluid density	1,020	kg/m ³
ρ_s	Solid density	2,650	kg/m ³
ϕ	Porosity	0.15	_

Note. the initial vertical stress, initial pressure and initial effective normal stress have been computed as: $\sigma_{yy}^0(y) = \left[(1 - \phi)\rho_s + \phi \rho_{fl} \right] g(y - D_0)$, where $\sigma_{yy}^0 < 0$, $p^0(y) = p_0^0 - \rho_{fl} g y$, $\sigma'^0(y) = \sigma^0(y) + \beta p^0(y)$. (Valid for reservoir, overburden and underburden.)

$$\sigma' = \sigma + \beta p,\tag{2}$$

where σ is the normal stress, β an effective stress factor (typically somewhat smaller than or equal to one) and p the reservoir pressure, that is, the pore pressure in the reservoir rock.

Equation 1 implies that slip of the hanging wall may occur in upward or downward direction, where exceedance of the slip stress τ_{sl} by a positive shear stress τ implies downward slip of the hanging wall, that is, a continued normal fault development. In this paper we only consider such downward slip without reversal of direction and therefore employ the usual definition of the pre-slip Coulomb stress

$$\tau_C = \tau - \tau_{sl},\tag{3}$$

in which slip corresponds to positive values of τ_C .

2.2. Fault Slip

Figure 4 (left) displays the pre-slip Coulomb stress τ_C in the fault. Positive values, indicated with green patches, result in (usually aseismic) fault slip δ as displayed in Figure 4 (middle). Figure 4 (right) displays the corresponding post-slip Coulomb stress $\check{\tau}_C$ which is just the sum of the pre-slip stress τ_C and the slip-induced stress $\check{\tau}$. It can be seen that at the locations where slip has occurred, the Coulomb stress has dropped to post-slip values equal

to zero. Because fault slip leads to a redistribution of shear stress, the slip patch boundaries (blue lines in the middle and right graphs) span a somewhat wider area than the pre-slip Coulomb stress zeros (green lines in the left graph). Continuing depletion will result in a gradual aseismic growth of the two slip patches until one of them (or occasionally both) becomes unstable and generates a seismic event which then also leads to merging of the patches. In another scenario, which seems to be less frequently occurring, the slip patches merge aseismically (Van den Bogert, 2018).

Using results from dislocation theory and fracture mechanics, it can be shown that the relationship between the pre-slip Coulomb stress and fault slip is governed by a convolution integral (Bilby & Eshelby, 1968; Rice, 1968; Segall, 2010; Weertman, 1996)

$$-\tau_C(y) = \text{PV } A \int_L \frac{\nabla \delta(\xi)}{\xi - y} d\xi, \ L = L_1 \cup L_2 \equiv (\tilde{y}_1, \tilde{y}_2) \cup (\tilde{y}_3, \tilde{y}_4), \tag{4}$$

where, for plane-strain conditions,

$$A = \frac{G}{2\pi(1-\nu)},\tag{5}$$

with G representing the shear modulus and ν Poisson's ratio, and

$$\nabla \delta(\xi) = \frac{\partial \delta(y)}{\partial y} \bigg|_{y=\xi},\tag{6}$$

with $\delta(y)$ representing the slip and $\nabla \delta(y)$ the slip gradient along the fault. The variables $\tilde{y}_i, i = 1, ..., 4$, in Equation 4 are horizontal projections on the y axis of the lower and upper slip patch boundaries \tilde{s}_i , where s is the along-fault coordinate (see Figure 3). In the remainder of this paper we will express all slip-related quantities, including frictional relationships, as function of the vertical coordinate $y = s \sin \theta$, where θ is the dip angle, rather than as function of the along-fault coordinate s to simplify the formulation. We emphasize that this has no effect on the numerical values of the stability analysis and the resulting expressions for the nucleation length, provided the analysis is restricted to faults with a constant value of θ (as is the case in our paper).

The prefix principal value (PV) in Equation 4 indicates that either of the integrands over L_1 and L_2 may become singular when $\xi = y$. The integral concerned is then a Cauchy-type singular integral and has to be interpreted in a PV sense (Estrada & Kanwal, 2000; Muskhelishvili, 1953). We will not indicate the singularity of integrals in the remainder of this paper, and therefore tacitly assume that they represent a PV whenever relevant.

2.3. Slip-Weakening Friction

In Equation 1 we used a constant friction coefficient. However, friction may be dependent on the accumulated slip, the slip rate, and one or more state variables (Ohnaka, 2013; Scholz, 2019). In case of slip-weakening friction, the value of the friction coefficient μ decreases as the slip δ increases in absolute value. Following Dascalu et al. (2000) and Uenishi and Rice (2003), we use a linear slip-weakening friction law which implies a linear decrease of the friction coefficient from a static value μ_s to a dynamic one μ_d over a critical slip distance δ_c ; see Figure 5. Disregarding cohesion, the Coulomb stress for slip-weakening friction can then be written as

$$\tau_{C}(y,\delta(y,p),p) = \tau(y,p) - \tau_{sl}(y,\delta(y,p),p)$$

$$= \tau(y,p) + \sigma'(y,p) \begin{cases} \left[\mu_{st} - (\mu_{st} - \mu_{dyn}) \frac{\delta(y)}{\delta_{c}} \right] & \text{if } |\delta(y)| \leq \delta_{c} \\ \mu_{dyn} & \text{if } \delta(y) > \delta_{c} \end{cases}$$
(7)

where we assume that $\tau > 0$ and $\delta \ge 0$, as is the case in the slip patches that develop during depletion of a normal-faulted reservoir, and using the sign convention discussed before in which compressive normal stresses are negative.

JANSEN AND MEULENBROEK 6 of 38

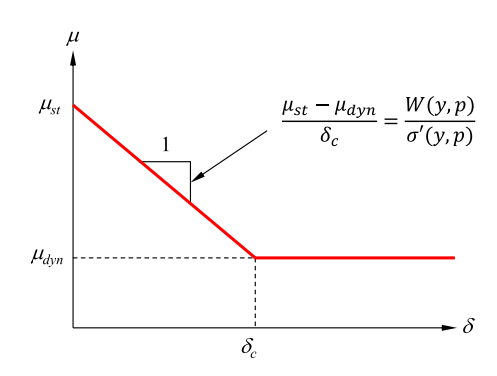


Figure 5. Slip-weakening friction law illustrated for positive values of δ . Unlike in the original Uenishi and Rice (2003) formulation, the value of W is varying over the slip patch because we consider a varying effective normal stress σ' .

Here, we also assume that always $\mu_{st} \ge \mu > \mu_{dyn}$ such that the horizontal branch in the slip weakening function is not reached, an assumption that is key in the derivation of the Uenishi and Rice criterion, but has to be verified for specific applications. Defining the auxiliary functions

$$R(y,p) = \tau(y,p) + \sigma'(y,p)\mu_{st}, \tag{8}$$

$$W(y,p) = -\sigma'(y,p) \left(\mu_{st} - \mu_{dyn}\right) / \delta_c, \tag{9}$$

Equation 4 can then be rewritten as

$$R(y,p) + W(y,p) \,\delta(y,p) = -A \int_{L(p)} \frac{\nabla \delta(\xi,p)}{\xi - y} \,d\xi, \ L(p)$$
$$= L_1(p) \cup L_2(p), \tag{10}$$

where we have now explicitly indicated that the length of the slip patches depends on the reservoir pressure p.

2.4. Onset of Seismicity

Instability in a fault during depletion occurs when an infinitesimal drop in pressure p leads to an unbounded growth of one or both of the slip patches L_1 and L_2 . The corresponding pressure p^* and patch length Δy^* are then, by definition, the nucleation pressure and the nucleation length. This process can be analyzed by considering the pressure derivative of Equation 10 which leads to

$$\dot{R}(y,p) + \dot{W}(y,p)\,\delta(y,p) + W(y,p)\,\dot{\delta}(y,p) = -A\int_{L(p)} \frac{\nabla \dot{\delta}(\xi,p)}{\xi - y} \,d\xi + B_i\left(y,\tilde{y}_i,\dot{\tilde{y}}_i,p\right),\tag{11}$$

where we used dotted variables to indicate differentiation with respect to pressure, and where B_i , $i=1,\ldots,4$, are terms resulting from differentiation of the integration boundaries \tilde{y}_i . It was shown in Jansen and Meulenbroek (2022) that the boundary terms vanish, and that for reservoir pressures approaching the nucleation pressure, the terms \dot{R} and $\dot{W}\delta$ become insignificant compared to $W\dot{\delta}$ such that we end up with

$$W(y,p)\dot{\delta}(y,p) = -A \int_{L(p)} \frac{\nabla \dot{\delta}(\xi,p)}{\xi - y} d\xi.$$
 (12)

Equation 12 is a generalized eigenproblem in terms of the slip rate $\dot{\delta}(y,p)$ and the slip gradient rate $\nabla \dot{\delta}(y,p)$. Uenishi and Rice (2003) considered a simpler version of Equation 12 for a single slip patch and with a term W that was independent of y and p, from which they derived closed-form expressions for Δy^* and p^* .

A single-patch solution can no longer accurately describe the onset of seismicity when depletion-induced stress peaks in a displaced fault are getting close enough to influence each other, a situation that occurs when the fault throw becomes greater than approximately 70 % of the reservoir height (Jansen & Meulenbroek, 2022). In this paper we therefore develop expressions for the onset of seismicity in displaced faults for situations where interaction between the patches cannot be ignored. In particular, we formulate an exact eigenvalue criterion and an extended version of the Uenishi and Rice (2003) criterion for coupled slip patches.

3. Solution Methods

3.1. Semi-Analytical Solutions and Numerical Integration

Singular integral equations such as (4) have been extensively considered in the literature on fracture mechanics (Bilby & Eshelby, 1968; Rice, 1968; Weertman, 1996). (Semi-) analytical solution methods make use of complex function theory (Muskhelishvili, 1953) or expansions in Chebyshev polynomials (Mason & Handscomb, 2003), while also various numerical integration methods have been developed of which one in particular, that is, augmented Gauss-Chebyshev quadrature, has been applied in publications on fault slip; see Multhopp (1938);



Journal of Geophysical Research: Solid Earth

10.1029/2025JB031577

Erdogan and Gupta (1972) and Kalandiya (1975) for detailed derivations, Erdogan (1978) for an extension to integrals over multiple domains, and Hills et al. (1996); Garagash and Germanovich (2012); Brantut and Viesca (2014); Bruhat and Segall (2017); Viesca and Garagash (2018) and Liu et al. (2019), among others, for further developments and applications to fracture and fault mechanics.

Appendix B provides the necessary elements of the theory of singular integrals as required for Appendices C and D which provide detailed derivations of the forward solution method and the exact and approximate eigenproblem solutions, both for single patches (or uncoupled double patches) and for coupled double patches. The key mathematical innovation involves the definition of a singular functional form of the slip gradient which allows for a formulation of the slip-patch end conditions that can be extended to multiple patches in a straightforward manner; see Sections C.1.2, C.1.4 and C.2.1 in Appendix C for details. The original formulation of Uenishi and Rice (2003) does not allow for such an extension. Supporting Information S1 contains details of the corresponding numerical implementation.

3.2. Simulation of Slip

In an earlier publication we approximated the development of slip and the onset of seismicity in a configuration in which the patches are approaching each other so closely that coupling can no longer be neglected (Jansen & Meulenbroek, 2022). Later, we developed a mathematically more rigorous approach to obtain an exact solution for the gradual development of slip in 'coupled double patches' (Meulenbroek & Jansen, 2024). In the latter paper, we introduced a modified version of augmented Gauss-Chebyshev quadrature which avoids matrix inversion and only requires numerical integration. This "inverse" approach is computationally superior to the regular "forward" version of augmented Gauss-Chebyshev quadrature, as long as the Coulomb friction remains independent of the slip. However, for slip-weakening friction, in which case the Coulomb friction becomes a function of the slip, an additional iterative procedure is required which becomes increasingly inefficient when the reservoir pore pressure approaches the nucleation pressure. Moreover, the inverse approach cannot be used to obtain an eigenvalue-based solution for the nucleation length.

For the current paper, we therefore return to the semi-analytical approach, starting from "forward" Equation 10, while making use of the findings of our "inverse" approach to incorporate the necessary auxiliary conditions and obtain an exact coupled solution for induced fault slip in a displaced fault in case of slip-weakening friction. As long as the slip remains smaller than the cut-off value δ_c (see Figure 5), this forward method is iteration-free. A key element in the derivation is a careful specification of the end conditions in the slip patches, with additional conditions to satisfy the integration constants in the underlying inverse formulation.

3.3. Fault Stability in Case of a Single Slip Patch

The papers by Dascalu et al. (2000) and Uenishi and Rice (2003) followed the semi-analytical route to study the development of slip and the onset of seismicity in the presence of slip-weakening friction, based on Equation 12 as applied to a slip patch with either an infinitesimal constant shear stress distribution (Dascalu et al., 2000) or a finite single-peaked distribution (Uenishi & Rice, 2003). Both papers considered fault stability with the aid of an eigenfunction expansion and a representation of Coulomb stress and slip in terms of Chebyshev polynomials. While Dascalu et al. (2000) focused on instability caused by perturbation of an already critically stressed fixed-length fault, Uenishi and Rice (2003) described the process of aseismic growth of a single slip patch and showed that nucleation occurs if the patch length reaches a critical value Δy_{eig}^* , with the corresponding pressure p then being called the nucleation pressure p^* . In both publications, W was assumed to be constant along the fault which allowed the authors to derive an eigenvalue criterion

$$\Delta y_{eig}^* = \Delta y_{U\&R}^* = 1.158 \frac{G}{W(1-\nu)}.$$
 (13)

Here, we use a subscript U&R to refer to the result of Uenishi and Rice (2003), but we note that the numerical value of 1.158 was already obtained in the analysis by Dascalu et al. (2000). In Section D.1 of Appendix D we used a slightly different approach to re-derive this expression, with a direct expansion in Chebyshev polynomials without an initial eigenfunction expansion.

JANSEN AND MEULENBROEK 8 of 38



Journal of Geophysical Research: Solid Earth

10.1029/2025JB031577

Van den Bogert (2018) and Buijze et al. (2019) noted that use of Equation 13 can be stretched to obtain approximate pressure-dependent values $\Delta y_{eig}(p)$ in case of a non-constant value of W(y,p), according to

$$\Delta y_{eig}(p) \approx \Delta y_{U\&R}(p) = 1.158 \frac{G}{\overline{W}(p) \cdot (1 - \nu)},$$
(14)

where $\overline{W}(p)$ is an averaged value over the slip patch,

$$\overline{W}(p) = \frac{1}{\Delta y(p)} \int_{\bar{y}}^{\bar{y}_{+}(p)} W(y, p) \, dy, \tag{15}$$

with $\Delta y(p) = \tilde{y}_+(p) - \tilde{y}_-(p)$ representing the patch length at pressure p. Exact values of the nucleation length Δy^* correspond to the pressure for which $\Delta y(p) = \Delta y_{eig}(p)$, which is then, by definition, the nucleation pressure p^* . Approximate values are therefore obtained for the pressure for which $\Delta y(p) = \Delta y_{U\&R}(p)$.

Van den Bogert (2018) and Buijze et al. (2019) used Equations 14 and 15 to identify the nucleation length during numerical simulations of depletion-induced fault slip, and aid the pressure step size selection which becomes very sensitive close to the nucleation pressure. We note that Uenishi and Rice (2003) derived an explicit expression for p^* , valid for the particular fault stress distribution in their paper. However, the "stretched" use of the Uenishi and Rice (2003) criterion does no longer allow for such a computation of p^* , and a simple gradual change of p, or a more sophisticated search strategy, is required to identify p^* .

Numerical experiments by Jansen and Meulenbroek (2022) for cases of depletion-induced seismicity with spatially varying effective stress along the fault confirmed that, for the examples considered, variations in the value of W(y,p) along the slip patch had only a small impact on the nucleation length, and that Equations 14 and 15 can therefore indeed be used to reliably approximate the nucleation length in numerical simulations in comparable parameter ranges. However, the results of Jansen and Meulenbroek (2022) also showed that this no longer holds when the two slip patches approach each other closely. In that case, the nucleation length rapidly drops with reducing distance between the patches, a feature that is neither captured in the original Uenishi and Rice (2003) criterion in Equation 13, nor in the modified version in Equation 14.

3.4. Fault Stability in Case of Coupled Slip Patches

The forward formulation developed in the current paper allows for an exact eigenvalue-based solution, and an approximate solution in the form of an "Extended Uenishi and Rice (EU&R) criterion" for the nucleation length in the coupled double-patch case. The exact result follows from Equation 12 as applied to a double-patch configuration, and requires additional "cross terms" to cope with the effect of the slip in one patch on the stresses in the other patch, and vice-versa. For these additional non-singular terms, which require a different treatment than the singular main terms, we derived exact analytical and numerical integral formulations; see Section D.2 in Appendix D for details.

The approximate Uenishi and Rice (U&R) solution for a single patch relied on the isolation of a single parameter which could be computed case-independently from the eigenproblem. For the coupled case, this isolation is no longer possible, and a similar EU&R expression becomes dependent on three parameters which, moreover, can only be determined through case-specific computations. To circumvent this problem we made use of the near-symmetry of the stress state in a displaced fault configuration with homogeneous rock properties properties: Figure 4 illustrates that in such a situation the Coulomb stress distributions and the slip pattern are almost symmetric around the line y = 0, where the slight asymmetry results from the change in initial pressure and initial stress gradients with depth. For large values of depth D_0 with respect to the reservoir height h, we can therefore approximate the slip patch pattern with the result for a symmetric configuration. This allows for an EU&R solution

$$\Delta y_{EU\&R}(p) = f(\hat{r}) \frac{G}{\overline{W}(p)(1-\nu)},\tag{16}$$

in terms of a single parameter

JANSEN AND MEULENBROEK 9 of 38

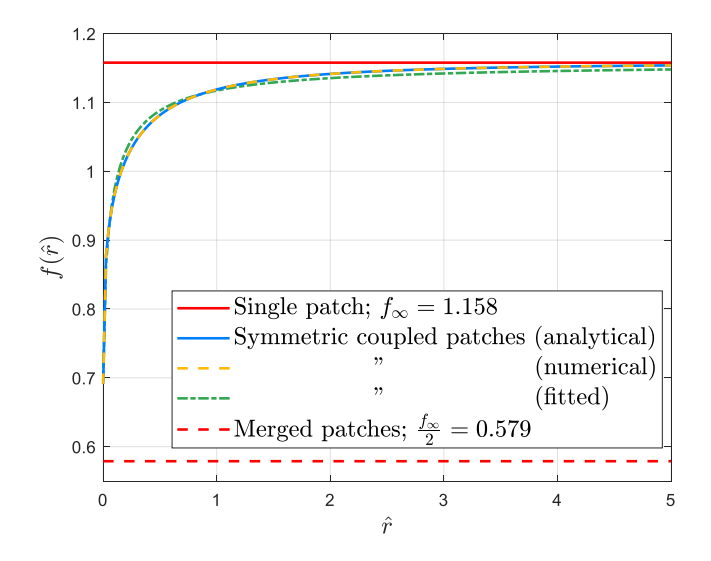


Figure 6. Value of factor $f(\hat{r})$ for use in the Extended Uenishi and Rice criterion as a function of the scaled (projected) distance \hat{r} between the symmetric slip patches. The solid red line represents $f_{\infty} = 1.158$ as used in the original Uenishi and Rice (2003) criterion for the single-patch case. The dashed red line represents $\frac{f_{\infty}}{2} = 0.579$.

$$\hat{r} = \frac{\tilde{y}_3 - \tilde{y}_2}{\tilde{y}_4 - \tilde{y}_3}, \quad 0 < \hat{r},\tag{17}$$

which represents the distance between the slip patches, scaled with the top slip patch length.

Figure 6 depicts the values of $f(\hat{r})$ as a function of \hat{r} for analytical and numerical results (in blue and orange respectively), and Figure 7 gives the same results on a logarithmic scale for an extended domain. See Section D.2 in Appendix D for computational details. The functional relationship for $f(\hat{r})$ has been tabulated in Supporting Information S2. Alternatively, it can be approximated as

$$f(\hat{r}) \approx f_{10^{-5}} + (f_{\infty} - f_{10^{-5}}) \left[\frac{2}{\pi} \operatorname{arcsec} (\hat{A} \hat{r}^{\hat{B}} + 1) \right],$$
 (18)

where

$$f_{10^{-5}} = 0.691$$
, $f_{\infty} = 1.158$, $\hat{A} = 6.357$ and $\hat{B} = 0.943$. (19)

We note that the arcsec function has no physical relevance and has been chosen pragmatically to fulfill the end point conditions. The values of fitting

parameters \hat{A} and \hat{B} have been determined through a least squares fit over $10^{-5} \le \hat{r} \le 10^2$; see the green dash-dotted lines in Figures 6 and 7.

The upper limit for $f(\hat{r})$ in these figures is equal to the value $f_{\infty} = f(\hat{r} \uparrow \infty) = 1.158$ that was found by Dascalu et al. (2000) and Uenishi and Rice (2003) for a single slip patch. The smallest value of \hat{r} for which numerical convergence of $f(\hat{r})$ can be obtained equals $\hat{r} = 10^{-5}$ for which we find $f(\hat{r}) = 0.691$; see Section D.2.5 in Appendix D for a detailed convergence analysis. The theoretical minimum for $f(\hat{r})$ is $\frac{f_0}{2} = 0.579$ because for $\hat{r} = 0$ the patches merge, at which moment the nucleation length is governed by the single-patch solution for the merged patches. However, both the average shear stress and the average shear resistance in a fault with two touching slip patches will have different magnitudes than those in a fault with a single slip patch of equal length, and the nucleation length for a touching double-patch configuration could therefore be above the theoretical minimum. In that case a further depletion may be accommodated, resulting in a further growth of the merged

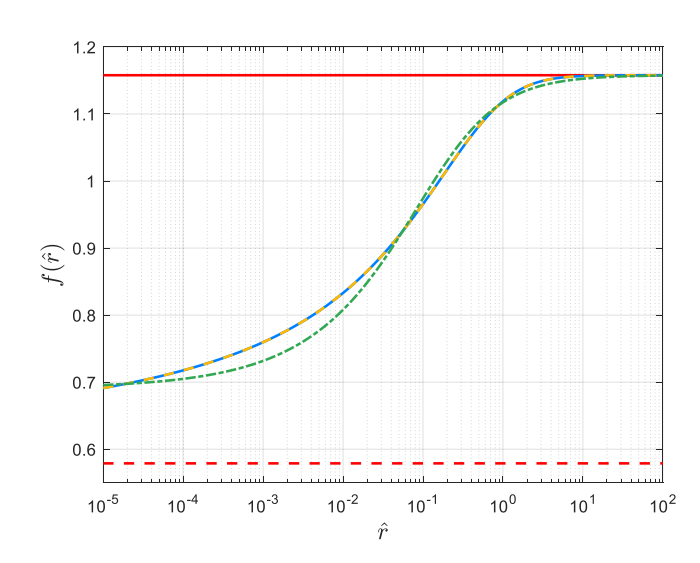


Figure 7. Identical results as in Figure 6 but represented on a logarithmic scale for $10^{-5} < \hat{r} < 10^2$. Legend as in Figure 6.

patches, before nucleation occurs. The results for small values of \hat{r} in Figure 7 suggest that the theoretical minimum will indeed not be reached. Moreover, the limiting case of merging before nucleation did show up in numerical simulations by Van den Bogert (2018) as well as in the numerical example discussed below.

3.5. Termination of Forward Simulations When Reaching Nucleation

Simulation to compute the slip patch boundaries $\tilde{y}_i, i=1,\ldots,4$, as a function of Δp can be efficiently performed with a variable-pressure-stepping algorithm. Close to nucleation this requires increasingly small pressure steps and tight tolerances on the iterative computation of the slip patch boundaries, to avoid overshooting the nucleation pressure p^* and, thus, the nucleation length Δy^*_{sim} . Termination of the simulation can be triggered when the (numerically computed) derivative $\frac{dp}{d\Delta y}$ drops below a pre-defined tolerance, but this approach is sensitive to numerical errors.

As an alternative, one can compute the value of $\Delta y_{eig}(p)$ when approaching nucleation and then terminate the simulation when $\Delta y_{sim}(p) \approx \Delta y_{eig}(p)$ (Jansen & Meulenbroek, 2022), while one could also terminate the simulation



Journal of Geophysical Research: Solid Earth

10.1029/2025JB031577

when $\Delta y_{sim}(p) \approx \Delta y_{EU\&R}(p)$. The use of the eigen value criterion is the preferred approach when the iterative semi-analytical inverse simulation procedure is used, for example, to cope with situations where slip values δ reach the cut-off value δ_c . The EU&R approximation then offers hardly any computational benefit while it is also slightly less accurate.

For the forward method without iteration, as formulated in this paper, simulation can robustly be terminated when Δy_{sim} starts to decrease instead of increase. This sign-reversal of the slip patch growth when reaching nucleation is a specific feature of this forward method. Also for this case, the EU&R approximation offers no advantages.

The EU&R criterion has therefore no practical value when used with a semi-analytical approach (whether inverse or forward). However, it may have value when used in combination with a fully numerical quasi-static computation of the onset of seismicity with the aid of, for example, a finite element, finite difference or finite volume code. The EU&R approximation can then be used as a simple and robust stopping criterion to avoid a time-consuming refinement of the depletion pressure increments close to the nucleation pressure, as was done by Van den Bogert (2018) and Buijze et al. (2019) for the uncoupled case.

4. Examples to Illustrate the Effect of Fault Offset

Figure 8 represents two examples with different values of the scaled fault offset

$$\tilde{t}_f = \frac{t_f}{h} = \frac{b-a}{a+b}. (20)$$

The two left graphs in Figure 8 display the pre-slip Coulomb stresses, and the two middle graphs the growth of the slip patches as a function of depletion, computed with the forward solution method for coupled patches. The two graphs on the right display the growth of the length of the top patch and show the moment at which it reaches the nucleation length as computed with the exact eigenvalue criterion for coupled patches (blue curve) and the approximation computed with the Extended Uenishi and Rice approach (green curve). In the small-offset case ($\tilde{t}_f = 0.33$), depicted in the top row of graphs, interaction between the patches is not important: the two slip patches grow with increasing depletion until the top one becomes unstable, and almost exactly the same result can be obtained with the uncoupled, single-patch formulation. The scaled patch distance \hat{r} is equal to 5.17 at nucleation. It can also be seen (in the top right graph) that the exact eigen-value-based and the approximate U&R results are hardly changing with increasing depletion. However, in the large-offset case ($\hat{t}_f = 0.84$), depicted in the bottom row of graphs, interaction does play a role and nucleation occurs earlier than if an uncoupled solution method would have been used. In this case, $\hat{r} = 0.069$ at nucleation. Moreover, the eigenvalue-based and EU&R criteria to compute the nucleation length are now increasingly influenced by depletion when approaching the nucleation pressure.

In the small-offset cases that we considered, nucleation always occurs in the top patch, as a result of the asymmetry in the pre-slip Coulomb stress distribution in which the top patch is slightly larger than the bottom patch. At that moment, the bottom patch is still somewhat away from nucleation; see Figure 8 (top) where the slope of the top curve at nucleation is near-vertical (although difficult to observe) whereas the slope of the bottom curve at that same pressure is still much flatter. However, in situations with a large fault offset, such that coupling becomes important, the slip in the bottom patch accelerates when the top patch approaches nucleation, with the effect that both patches loose stability at (almost) the same moment in time; see Figure 8 (bottom) where both curves now have a clearly-visible near-vertical slope at nucleation.

Figure 9 gives a detailed view of the pre-slip Coulomb stress τ_C , the slip gradient $\nabla \delta$ and the slip δ for the large-offset case, for increasing absolute values of incremental pore pressure Δp . Note that in the plot for δ , the maximum slip values are nearly equidistant. However the corresponding values of Δp are increasingly closely spaced. In other words, the effect of pore pressure decrease becomes increasingly strong when approaching the nucleation limit.

Figure 10 depicts the nucleation pressure Δp^* (top), the corresponding nucleation length Δy^* (middle) and the maximum slip δ_{\max}^* (bottom) as function of \tilde{t}_f . The small-offset case ($\tilde{t}_f = 0.33$) and large-offset case ($\tilde{t}_f = 0.84$) have been indicated with vertical dash-dotted lines. It can be seen in the top graph that an increase in fault throw results in a gradual decrease in absolute nucleation pressure (solid red dots). For very low values of \tilde{t}_f , depletion

JANSEN AND MEULENBROEK 11 of 38

21699356, 2025, 10, Downloa

ded from https://agupubs.onlinelibrary.wiley.com/doi/10.1029/2025JB031577 by Technical University Delft, Wiley Online Library on [30/10/2025]. See the Terms

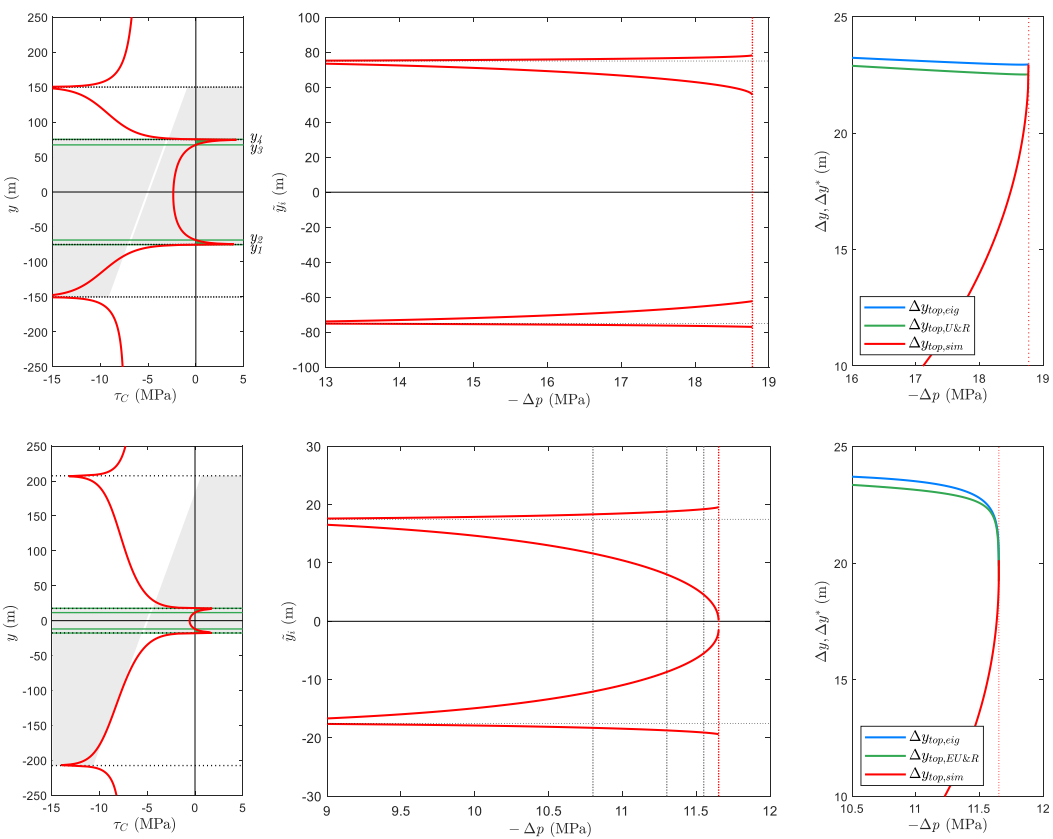


Figure 8. Aseismic slip and nucleation. Left column: pre-slip Coulomb stress τ_C over the height of the reservoir; gray areas indicate the footwall and the hanging wall. Middle column: slip patch boundaries \tilde{y}_i , $i = 1, \dots, 4$, as a function of pore pressure change Δp . Right column: Top slip patch length $\Delta y_{sim}(p)$, and pressure-dependent estimates of the nucleation length $\Delta y_{eig}(p)$ (from the exact eigenvalue approach) and $\Delta y_{(E)U\&R}(p)$ (from the (Extended) Uenishi and Rice criterion) as a function of Δp . Top row: small-offset case; fault throw $t_f = 75$ m ($\mathfrak{F} = 0.33$); no noticeable coupling effect; τ_C displayed for $\Delta p = -18.7755$ MPa; nucleation occurs at $\Delta p = -18.7758$ MPa. Bottom row: large-offset case; fault throw $t_f = 190$ m $(\tilde{f}=0.84)$; clear coupling effect; τ_C displayed for $\Delta p=-11.6511$ MPa; nucleation occurs at $\Delta p=-11.6512$ MPa. The vertical gray and red dotted lines correspond to the incremental pressures used to generate Figure 9. Be aware of the different vertical scales of the graphs in the middle column. Parameter values as in Table 1.

up to -30 MPa is not enough to trigger nucleation (open red dots). For high values of \tilde{t}_f , merging of the patches occurs before the nucleation pressure is reached (red-edged blue and solid blue dots).

The middle graph in Figure 10 shows that the nucleation length stays near-constant until around $\tilde{t}_f = 0.70$ when a rapid decline results from the coupling effect. The red dots represent simulation results Δy_{sim}^* , the blue triangles eigenvalue results Δy^*_{eig} , and the green dots EU&R approximations $\Delta y^*_{EU\&R}$. Just as in the top graph, for high values of \tilde{t}_f , merging occurs before the nucleation length is reached. For the first three merged cases, merging immediately results in an exceedance of the single-patch nucleation length such that there is no practical difference between nucleation leading to merging, or merging leading to nucleation (red-edged blue dots). Only for the last three cases, merging does not result in seismicity immediately after merging (blue dots). A slight further depletion is then possible, resulting in a further growth of the merged patches, before reaching the single-patch nucleation length. The simulation results (red dots) were obtained by terminating the forward simulation when the growth of the slip patch length reversed sign, and the red dots represent the last value of Δy_{sim}^* just before the sign reversal; they almost coincide with the Δy_{eig}^* values (blue triangles). The small deviation of the EU&R results (green dots) from the eigenvalue-based results stems from the compound effects of assuming a symmetric Coulomb stress distribution, using an averaged value \overline{W} , and approximating $f(\hat{r})$ with the least-squares fit described in Section 3.4.

21699356, 2025, 10, Downlo

ded from https://agupubs.onlinelibrary.wiley.com/doi/10.1029/2025JB031577 by Technical University Delft, Wiley Online Library on [30/10/2025]. See the

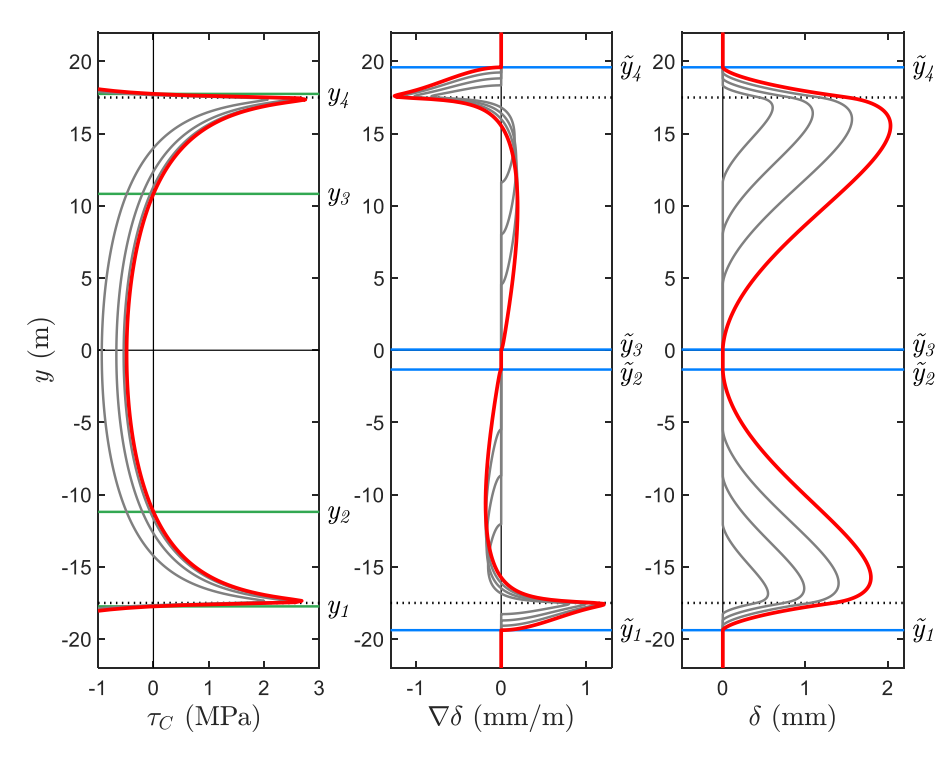


Figure 9. Detailed view of pre-slip Coulomb stress, slip gradient and slip, at four incremental pressure values for the large-offset case of Figure 8. Left: pre-slip Coulomb stress τ_C . Middle: slip gradient $\nabla \delta$. Right: slip δ . The values of the incremental pressure are $\Delta p = -10.80, -11.30, -11.55$ and -11.6511 MPa with the first three indicated in gray and the last one in red.

The bottom graph in Figure 10 just serves to illustrate that the maximum observed fault slip δ_{\max}^* occurs for $t_f = 20 \,\mathrm{m} \left(\tilde{t}_f = 0.09 \right)$ and is less than 8 mm which is far below the cut-off value $\delta_c = 20 \,\mathrm{mm}$ above which linear slip weakening would no longer be valid. Use of the forward method, the eigenvalue approach and the EU&R criterion as developed in our paper are therefore justified for the examples considered.

Figure 2 illustrates that occasionally faults are encountered with a scaled offset larger than one, such that the reservoir segments at the left and right sides of the fault are no longer in contact. It has been shown numerically by Van den Bogert (2018) that in case of equal depletion in the left and right reservoir segments, the absolute incremental pressure at nucleation $|\Delta p^*|$ is increasing again for increasing values of $1 < \tilde{t}_f$ (Van den Bogert, 2018, Ch.4). The theory developed in our paper is also valid for such a situation, but we did not further analyze this special case, and the exact functional form of $f(\hat{r})$ for $1 < \hat{t}_f$ remains to be determined.

We note that the examples in our paper are computed for near-steady state and spatially constant reservoir pressures. However, this is by no means a necessary condition. The stability analysis and resulting expressions for the nucleation length are also valid for time-varying fault stresses, for example, resulting from pore pressure fluctuations, as long as inertia effects do not play a role. Moreover, the fault stresses may result from spatially varying reservoir depletion. An essential requirement, however, is spatial uniformity of the elastic constants, both inside and outside the reservoir.

Caveat: the parameter values in the examples discussed in this section have been chosen to roughly represent those of the Groningen natural gas field (NAM, 2016), but we acknowledge that the examples represent a strongly simplified view of reality. The limitation to two dimensions, elastic behavior, a slip-weakening friction law, and the disregard of a more complex fault geometry with gouge, near-fault damage and heterogeneous material properties may all be challenged. The examples are therefore primarily meant to illustrate the features of the EU&R criterion for this specific parameter range.

ary.wiley.com/doi/10.1029/2025/B031577 by Technical University Delft, Wiley Online Library on [30/10/2025]. See the Terms

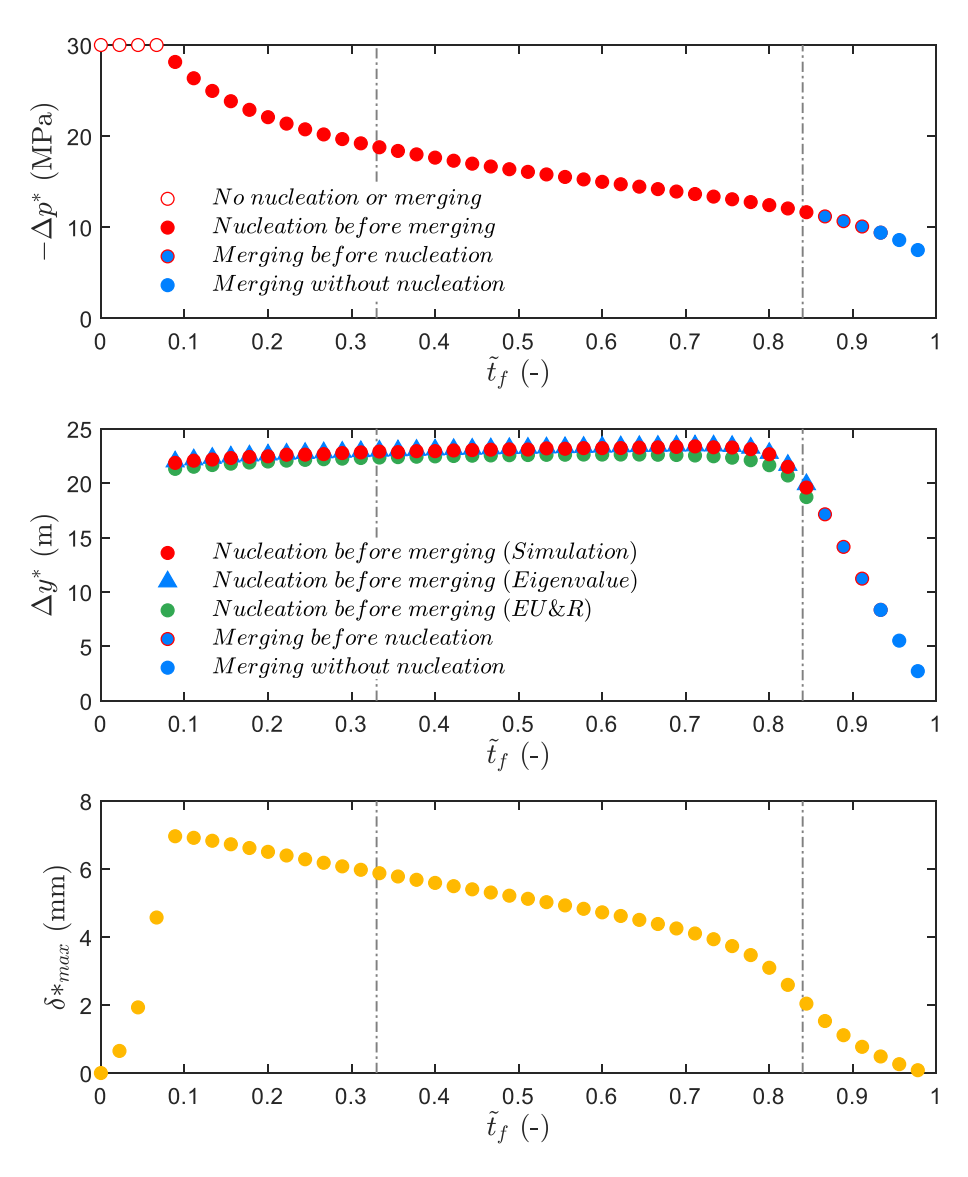


Figure 10. Nucleation pressure $-\Delta p^*$ (top), nucleation length Δy^* (middle) and maximum slip at nucleation δ_{\max}^* (bottom) as a function of scaled fault offset \tilde{I}_f . Parameter values as in Table 1.

5. Overview and Conclusions

We re-derived the stability criterion for the onset of seismicity in a fault with slip-weakening friction and loaded with a single-peaked shear stress, as originally formulated by Uenishi and Rice (2003) who build on earlier work by Dascalu et al. (2000). Our aim was to extend this criterion for use in faults loaded by a double-peaked shear stress in which the peaks are close enough to influence each other's shear stress distribution. We specifically considered the stress pattern that occurs during depletion of a reservoir intersected by a displaced normal fault, that is, a fault with a finite offset. We first formulated a forward solution strategy to compute the four boundaries of the two slip patches as a function of depletion pressure. We subsequently formulated an eigenproblem to derive the exact nucleation length Δy_{eig}^* for a single-patch (or two patches without coupling), that is, the maximum slip patch length that can be sustained without losing stability of (one of) the slip patches.

Both the forward and the eigenproblem formulation rely on a reformulation of the original Uenishi and Rice (2003) problem, which results in a much more straightforward derivation that can, moreover, be extended to two or more coupled slip patches unlike the original formulation. An aspect of the double-patch formulation is the

JANSEN AND MEULENBROEK 14 of 38

appearance of non-singular "cross terms" that quantify the effect of slip in one patch on the stresses in the other patch and vice versa, for which we derived dedicated numerical and exact analytical integral formulations.

For the single-patch case (or a double-patch case without coupling) with a constant normal stress along the fault, it is possible to formulate the eigenproblem in terms of a single dimensionless parameter \tilde{w} , representing the scaled slope of the slip-weakening friction law, which allows for a simple expression for the nucleation length as originally derived by Uenishi and Rice (2003) (and, in a slightly different setting, also by Dascalu et al. (2000)),

$$\Delta y_{U\&R}^* = 1.158 \ \frac{G}{W(1-\nu)},\tag{21}$$

where G is the shear modulus, W the slope of the slip weakening friction law times the effective normal stress, and ν Poisson's ratio.

For the coupled double-patch case with a non-constant normal stress along the fault, we successfully obtained the exact eigen solution Δy_{eig}^* . For the same case with a constant normal stress along the fault, the corresponding eigenproblem depends on three dimensionless parameters which, however, cannot be isolated from the governing equations. A simple U&R-like expression for the general asymmetric case is therefore out of reach. In case of a symmetric double-patch configuration with a constant normal stress, the eigenproblem depends on \tilde{w} and only one additional dimensionless parameter \hat{r} , representing the distance between the slip patches scaled with the patch length. Moreover, \tilde{w} can now be isolated again, and this allows for the derivation of an Extended Uenishi and Rice (EU&R) criterion:

$$\Delta y_{EU\&R}^* = f(\hat{r}) \frac{G}{W(1-\nu)},\tag{22}$$

where the function $f(\hat{r})$ has been tabulated (see Supporting Information S1) and can be approximated in closed form with Equation 18. We note that the value of \hat{r} depends on the yet unknown nucleation pressure p^* , which means that it is necessary to gradually reduce the incremental pressure Δp , or use another search strategy, to find the value of p^* that corresponds to the nucleation length $\Delta v^*(p^*)$.

As observed earlier by Van den Bogert (2018) and Buijze et al. (2019), the U&R criterion can also be used to approximate the nucleation length in case of a non-constant normal stress along the fault. A similar approximation can be made with the EU&R criterion. In those cases, the nucleation length becomes a function of the average value $\overline{W}(p)$ of W(y,p) over the slip patch, which, in our application, is a function of the reservoir pressure p. Also such a "stretched" use of the (E)U&R criterion (with varying normal stress) therefore requires a gradual pressure reduction, or another search strategy, to find the nucleation pressure p^* .

We considered examples with parameter values roughly resembling those of the Groningen natural gas field, leading to near-symmetric stress distributions and approximate nucleation lengths $\Delta y_{EU\&R}^*$ that closely match the exact eigenvalue-based solutions Δy_{eig}^* . For these examples, the effect of coupling between slip patches starts to play role for situations where the fault offset exceeds approximately 70% of the reservoir height.

The results of our analysis show that nucleation of depletion-induced seismicity in a faulted reservoir will occur somewhat earlier when the interaction between slip patches is taken into account than when it is neglected. However, this effect is limited to faults with a large offset relative to the reservoir height while it also depends on parameters that are highly uncertain in practice. Further work, involving rupture simulations and comparisons with actual observed seismicity, will therefore be required to assess the effect on seismic magnitudes and the practical relevance (if any) of the theoretical results obtained in our paper. Nevertheless, the mathematical approach to quantify the effect of slip patch interaction on nucleation length can be extended to multiple patches and could therefore form a useful tool to investigate the development of fault slip in more complex settings.

Moreover, a practical application of the EU&R criterion derived in our paper could be to serve as a robust codeindependent termination criterion during the numerical simulation of depletion-induced fault slip resulting from natural gas or geothermal energy production, using, for example, a finite element, finite difference or finite volume code; or as an indicator of approaching nucleation in an adaptive pressure stepping scheme during such

16 of 38

Table 2 Nucleation Criteria				
Patch Configuration	Effective normal stress	Nucleation criterion	Dependent on p ?	Simulator-independent ?
Single	Constant	$\Delta y_{U\&R}$ (original)	No	Yes
Single	Non-constant	$\Delta y_{U\&R}$ (stretched)	Yes	Yes
Single	Non-constant	Δy_{eig}	Yes	No
Double	Constant	$\Delta y_{EU\&R}$	Yes	Yes
Double	Non-constant	$\Delta y_{EU\&R}$ (stretched)	Yes	Yes
Double	Non-constant	Δy_{eig}	Yes	No

simulations to help avoiding excessive pressure step size reductions close to the nucleation pressure. Table 2 gives an overview of the various nucleation criteria for single-patch and double-patch configurations with or without constant effective normal stress in the patches. The last column shows if the criterion can be used as a simulator-independent stand-alone criterion.

Appendix A: Closed-Form Expressions for Induced Fault Slip

This appendix describes the expressions that were used to compute the results displayed in Figure 4 (left). The material in this appendix has mostly been taken from Meulenbroek and Jansen (2024) and is included here for easy reference.

A1. Combined Stresses

The combined normal stress σ , shear stress τ and pressure p as used in this paper are the sum of initial components (indicated with a superscript zero) and incremental components (indicated with a prefix Δ):

$$\tau = \tau^0 + \Delta \tau, \quad \sigma = \sigma^0 + \Delta \sigma, \quad p = p^0 + \Delta p.$$
 (A1)

The initial components depend on the burial depth of the reservoir and the regional geological stress regime and may be considered constants. The incremental components result from human-induced activities where induced pressures subsequently lead to induced stresses, with positive values of Δp corresponding to fluid injection and negative values to depletion. We employ the solid mechanics sign convention where positive strains and stresses imply extension and tension. For a deep subsurface situation, combined normal stresses are always compressive and therefore negative-valued.

A2. Initial Stresses

We assume the presence of an initial regional stress pattern with principal stresses σ_{vv}^0 (vertical) and

$$\sigma_{xx}^{0} = \sigma_{xx}^{0} - \alpha p^{0} = K^{0} \sigma_{yy}^{0} - \alpha p^{0} = K^{0} (\sigma_{yy}^{0} + \alpha p^{0}) - \alpha p^{0}, \tag{A2}$$

(horizontal), where α is Biot's coefficient (typically somewhat smaller than one), p^0 is the initial pore pressure (a superscript "0" means "initial"), K^0 is the initial effective stress ratio, and where a primed stress variable σ' represents an "effective stress." The resulting initial normal and shear stresses acting on the fault follow from a coordinate rotation as

$$\sigma^0 = \sigma_{\tilde{y}\tilde{y}}^0 = \sigma_{xx}^0 \sin^2 \theta + \sigma_{yy}^0 \cos^2 \theta, \tag{A3}$$

$$\tau^0 = -\sigma_{xx}^0 = (\sigma_{xx}^0 - \sigma_{yy}^0) \sin \theta \cos \theta, \tag{A4}$$

where \tilde{x} and \tilde{y} are rotated coordinates, and where θ is the dip angle of the fault; see Figure 3. A positive-valued shear stress τ^0 corresponds to a normal faulting regime, that is, a situation where the hanging wall (to the left of the fault in Figure 3) has a tendency to slide down from the foot wall (to the right of the fault). The initial effective normal stress acting at the fault follows as

$$\sigma'^0 = \sigma^0 + \beta p^0, \tag{A5}$$

where β is an effective stress coefficient which is not necessarily identical to α and is often taken as unity (Fjaer et al., 2021; Scholz, 2019).

A3. Incremental Stresses

An increase or decrease in pore pressure in the reservoir will result in incremental normal and shear stresses in the reservoir and its surroundings because of poroelastic effects (Biot, 1941; Segall, 1989; Wang, 2000). We restrict the analysis in this paper to the case of a quasi steady state, that is, a situation with a spatially homogeneous incremental pore pressure $\Delta p(t)$ that is a slow function of time t. Using inclusion theory or the closely-related nucleus of strain method, it is possible to (semi-)analytically compute the incremental strains and stresses, inside and outside the reservoir, that result from a change in reservoir pore pressure Δp (Geertsma, 1973; Rudnicki, 2011; Segall, 1989).

Closed-form analytical expressions for incremental normal and shear stresses in a displaced fault were obtained by Cornelissen et al. (2024), Jansen et al. (2019), Lehner (2019), and Wu et al. (2021) with the aid of inclusion theory. For an inclined fault we have

$$\Delta \sigma = (-\Delta \sigma_{xy} \sin \theta \cos \theta + \Delta \sigma_{xx} \sin^2 \theta), \tag{A6}$$

$$\Delta \tau = (\Delta \sigma_{xy} \sin^2 \theta + \Delta \sigma_{xx} \sin \theta \cos \theta), \tag{A7}$$

where $\Delta \sigma_{xx} = \Delta \sigma_{\tilde{y}\tilde{y}}$ and $\Delta \sigma_{xy} = -\Delta \sigma_{\tilde{x}\tilde{y}}$ are normal and shear stresses for a vertical fault, that is, for a dip angle $\theta = \frac{\pi}{2}$. For an infinitely wide reservoir, these are defined as (Meulenbroek & Jansen, 2024)

$$\Delta \sigma_{xx} = -C \left\{ \arctan 2 \left[(a+b)\eta, \eta^2 + (y-b)(y+a) \right] + \arctan 2 \left[(a+b)\eta, \eta^2 + (y-a)(y+b) \right] \right\},$$
(A8)

$$\Delta \sigma_{xy} = \frac{C}{2} \ln \frac{\left[\eta^2 + (y-a)^2\right] \left[\eta^2 + (y+a)^2\right]}{\left[\eta^2 + (y-b)^2\right] \left[\eta^2 + (y+b)^2\right]},\tag{A9}$$

where the "arctan2" operation is defined for arguments (y,x) in the interval $[-\pi,\pi]$ according to

$$\arctan 2(y,x) = \begin{cases} \operatorname{sgn}(y) \cdot \arctan\left(\left|\frac{y}{x}\right|\right) & x > 0 \\ \operatorname{sgn}(y) \cdot \frac{\pi}{2} & x = 0, y \neq 0 \\ \operatorname{undefined} & x = 0, y = 0 \end{cases}$$

$$\operatorname{sgn}(y) \cdot \left[\pi - \arctan\left(\left|\frac{y}{x}\right|\right)\right] & x < 0$$
(A10)

and where a and b are defined in Figure 3, C is a pressure-dependent scaling parameter, with SI units Newton per meter squared, defined as

$$C = \frac{(1 - 2\nu)\alpha\Delta p(t)}{2\pi(1 - \nu)},\tag{A11}$$

JANSEN AND MEULENBROEK 17 of 38

with ν representing Poisson's ratio, and η is a regularization parameter with dimension "length" which serves to avoid jump discontinuities and singularities in Equations A8 and A9 respectively. The corresponding incremental effective normal stress is given by

$$\Delta \sigma' = \Delta \sigma + \beta \Delta p^r = \Delta \sigma + \beta \frac{\Delta p}{\pi} \arctan 2 \left[2b\eta, \eta^2 + (y - b)(y + b) \right]. \tag{A12}$$

Expressions for the limiting case where $\eta\downarrow 0$ are given in Meulenbroek and Jansen (2024). In the derivation of Equation A12 it was assumed that only those parts of the fault that are in direct contact with the reservoir experience incremental reservoir pressure, that is, that the relevant fault segment is given by -b < y < b. If a larger part of the fault is exposed to incremental pressure, the domain where $\beta\Delta p$ is added should be extended accordingly.

We note that these expressions are valid for an infinite elastic domain with uniform elastic parameters. Therefore, they do not take into the account the free-surface effect, which is fully justified if the reservoir height h is much smaller than the reservoir depth D_0 (Lehner, 2019; Wu et al., 2024).

Appendix B: Singular Integral Equations

B1. Generic Formulation

We use generic functions f(y) and g(y) to define the governing integral equations. In case of a single-peaked stress distribution, resulting in a single slip patch, we can then write

$$PV \int_{L} \frac{g(\xi)}{\xi - y} d\xi = f(y), \ L = (\tilde{y}_{-}, \tilde{y}_{+}), \tag{B1}$$

where f is known and g is to be determined, and where the prefix PV indicates that the principle value of the integral is implied because of its singularity for $\xi = y$. Equation B1 may also be used for a double-patch situation in which the interaction between the patches can be neglected. In that case we have either $(\tilde{y}_-, \tilde{y}_+) = (\tilde{y}_1, \tilde{y}_2)$, for the bottom patch, or $(\tilde{y}_-, \tilde{y}_+) = (\tilde{y}_3, \tilde{y}_4)$, for the top patch; see the patch configuration in Figure 4 (middle). In case of a double-peaked distribution with interaction, we write

$$PV \int_{L} \frac{g(\xi)}{\xi - y} d\xi = f(y), \ L = L_1 \cup L_2 \equiv (\tilde{y}_1, \tilde{y}_2) \cup (\tilde{y}_3, \tilde{y}_4).$$
 (B2)

Just like in the main text, we will refrain from using the indication PV in the remainder of this appendix.

If the known function g is Hölder-continuous (a somewhat stricter requirement than regular continuity) it can be shown that the inverse of Equation B1 is given by (Estrada & Kanwal, 2000; Muskhelishvili, 1953)

$$g(y) = \frac{1}{\pi^2 \Phi(y)} \int_L \frac{\Phi(\xi) f(\xi)}{\xi - y} d\xi + \frac{C_0}{\pi^2 \Phi(y)},$$
 (B3)

where

$$\Phi(y) = \sqrt{-(y - \tilde{y}_{-})(y - \tilde{y}_{+})}, \tag{B4}$$

while the inverse of Equation B2 can be expressed as

$$g(y) = \frac{1}{\pi^2 \Psi_+(y)} \int_I \frac{\Psi_\pm(\xi) f(\xi)}{y - \xi} d\xi + \frac{C_0 + C_1 y}{\pi^2 \Psi_+(y)},$$
 (B5)

where

$$\Psi_{\pm}(y) = \pm \sqrt{-(y - \tilde{y}_1)(y - \tilde{y}_2)(y - \tilde{y}_3)(y - \tilde{y}_4)},\tag{B6}$$

with the plus and minus signs preceding the square-root term corresponding to $y \in L_2$ and $y \in L_1$ respectively.

The coefficients C_0 and C_1 in the inverse equations can be determined by requiring that the integrals $\int \nabla \delta dy$ over the individual slip patches vanish (Meulenbroek & Jansen, 2024). Moreover, a physically realistic solution for the slip δ requires vanishing of the slip gradient $\nabla \delta$ at the slip patch boundaries (Bilby & Eshelby, 1968). In terms of generic functions, we therefore have to consider the auxiliary conditions

$$g(\tilde{y}_i) = 0, (B7)$$

$$\int_{L_i} g(y) \, dy = 0,\tag{B8}$$

where i = 2 and j = 1 for the single-patch case, and i = 4 and j = 2 for the double-patch case.

In this paper we consider the dependence of g(y,p) and its integral $G = \int g(y,p) dy$ on a parameter p in the known function f(y,p), where g, G, f and p represent the (scaled) slip gradient, slip, Coulomb stress and reservoir pressure respectively. We are particularly interested in situations in which the solution becomes unstable in the sense that an infinitesimally small change in p results in an unbounded growth of G (i.e., the onset of seismicity), a situation that may occur if the Coulomb stress is a slip-weakening function of the slip. This corresponds to solving a generalized eigenproblem that can be expressed generically as

$$\int_{L} \frac{g(\xi, p)}{\xi - y} d\xi = \lambda G(y, p), \tag{B9}$$

subject to auxiliary conditions (B7) and (B8).

B2. Gauss-Chebyshev Quadrature

We will make use of the following Gauss-Chebyshev quadrature formulas to integrate regular integrals (Mason & Handscomb, 2003):

$$\int_{-1}^{1} \frac{F(z)}{\sqrt{1-z^2}} dz \approx \sum_{m=1}^{M} \frac{\pi}{M} F(z_m),$$
 (B10)

$$\int_{-1}^{1} \sqrt{1 - z^2} F(z) dz \approx \sum_{n=1}^{N} \frac{\pi (1 - z_n^2)}{N + 1} F(z_n),$$
 (B11)

where the "first-kind Chebyshev points" z_m and the "second-kind points" z_n are defined as the zeros of the firstkind and second-kind Chebyshev polynomials $T_M(z)$ and $U_N(z)$ respectively:

$$z_m = \cos\frac{(m - \frac{1}{2})\pi}{M}, \ m = 1, \dots, M,$$
 (B12)

$$z_n = \cos\frac{n\pi}{N+1}, \ n = 1, \dots, N.$$
 (B13)

Moreover, we will use augmented Gauss-Chebyshev quadrature to integrate a singular integral according to (Erdogan & Gupta, 1972; Multhopp, 1938)

$$\int_{-1}^{1} \frac{F(\zeta)}{\sqrt{1-\zeta^2} (\zeta-z)} d\zeta \approx \sum_{m=1}^{M} \frac{\pi}{M} \frac{F(\zeta_m)}{\zeta_m - z_p},$$
(B14)

JANSEN AND MEULENBROEK 19 of 38 where ζ_m are regular first-kind Chebyshev points, which were already defined in Equation B12, and z_p are auxiliary points, located in between the regular points, defined as

$$z_p = \cos \frac{p\pi}{M}, \ p = 1, \dots, M - 1.$$
 (B15)

Appendix C: Forward Method

C1. Single Slip Patch

C1.1. Scaling

We define the "half length" y of the slip patch and its average position \bar{y} as

$$\underline{y} = \frac{\tilde{y}_{+} - \tilde{y}_{-}}{2}, \quad \bar{y} = \frac{\tilde{y}_{-} + \tilde{y}_{+}}{2}, \tag{C1}$$

and we introduce the scaled variables

$$z(y; \underline{y}, \overline{y}) = \frac{y - \overline{y}}{y} \Rightarrow y = \underline{y}z + \overline{y}, \tag{C2}$$

$$\zeta\left(\xi;\underline{y},\bar{y}\right) = \frac{\xi - \bar{y}}{y} \Rightarrow \xi = \underline{y}\zeta + \bar{y},\tag{C3}$$

to rewrite Equation B1 as

$$\tilde{f}(z;\underline{y},\bar{y}) = f(y = y(z);\underline{y},\bar{y}), \ \tilde{g}(\zeta;\underline{y},\bar{y}) = g(\xi = \xi(\zeta);\underline{y},\bar{y})$$
(C4)

resulting in

$$\int_{-1}^{1} \frac{\tilde{g}(\zeta)}{\zeta - z} d\zeta = \tilde{f}(z),\tag{C5}$$

with inverse formula

$$\tilde{g}(z) = \frac{1}{\pi^2 \widetilde{\Phi}(z)} \int_{-1}^1 \frac{\widetilde{\Phi}(\zeta) \tilde{f}(\zeta)}{\zeta - z} d\zeta + \frac{\widetilde{C}_0}{\pi^2 \widetilde{\Phi}(z)}, \tag{C6}$$

where

$$\tilde{\Phi}(z) = \sqrt{1 - z^2}, \ \tilde{C}_0 = \frac{C_0}{y}.$$
 (C7)

Furthermore, we introduce the scaled variables

$$\tilde{\delta}(z; p, \underline{y}, \overline{y}) = \frac{\delta(y = y(z; \underline{y}, \overline{y}), p)}{y},$$
(C8)

$$\tilde{w}(z; p, \underline{y}, \bar{y}) = \frac{W(y = y(z; \underline{y}, \bar{y}), p) \cdot \underline{y}}{A}, \tag{C9}$$

JANSEN AND MEULENBROEK 20 of 38

$$\tilde{r}\left(z;p,\underline{y},\bar{y}\right) = \frac{R\left(y = y\left(z;\underline{y},\bar{y}\right),p\right)}{A},\tag{C10}$$

where

$$A = \frac{G}{2\pi(1-\nu)},\tag{C11}$$

and view p, \underline{y} and \overline{y} as parameters. We aim to solve the problem for a (number of) given value(s) of p, while the parameters \underline{y} and \overline{y} will be determined as part of the solution. In the remainder of this appendix, we will suppress the dependence of the dependent variables on the parameters in the notation to improve readability, and we write the rescaled Equation 10, as applied to a single patch, as

$$\tilde{r}(z) + \tilde{w}(z)\tilde{\delta}(z) = -\int_{-1}^{1} \frac{d\tilde{\delta}}{\zeta - z} d\zeta, \tag{C12}$$

Note that all variables in Equation C12 are now dimensionless.

C1.2. Functional Form of the Slip Gradient

Equation C12 is equivalent to Equation C5 if we choose

$$\tilde{g}(\zeta) = -\frac{d\tilde{\delta}}{d\zeta} \text{ and } \tilde{f}(z) = \tilde{r}(z) + \tilde{w}(z) \,\tilde{\delta}(z),$$
 (C13)

which allows us to apply Equation C6 to derive an expression for the scaled slip gradient $\frac{d\tilde{b}}{dz}$:

$$\frac{d\tilde{\delta}}{dz} = -\frac{1}{\pi^2 \widetilde{\Phi}(z)} \left\{ \int_{-1}^1 \frac{\widetilde{\Phi}(\zeta) \left[\tilde{r}(\zeta) + \tilde{w}(\zeta) \, \tilde{\delta}(\zeta) \right]}{\zeta - z} \, d\zeta + \tilde{C}_0 \right\}. \tag{C14}$$

Equation C14 cannot be used to compute $\tilde{\delta}$ or $\frac{d\tilde{\delta}}{dz}$ directly. We do however observe that the slip gradient has the following form

$$\frac{d\tilde{\delta}}{dz} = \frac{h(z)}{\sqrt{1 - z^2}},\tag{C15}$$

where h(z) is a continuous function, because the term between brackets in Equation C14 is continuous. We can use a Taylor expansion of h(z) and then factorize as follows

$$h(z) = r_0 + r_1 z + (1 - z^2)(b_0 + b_1 z + \dots),$$
(C16)

where both the remainder $r_0 + r_1 z$ and the coefficients b_i can (in principle) be found by long division of h(z) by $1 - z^2$. This means that we obtain the following functional form for the slip gradient

$$\frac{d\tilde{\delta}}{dz} = \frac{r_0 + r_1 z + (1 - z^2)(b_0 + b_1 z + \dots)}{\sqrt{1 - z^2}}.$$
 (C17)

In order to have a finite derivative values at the end points of the slip patch, as required in condition (B7), we now require

$$r_0 = 0$$
 and $r_1 = 0$. (C18)

JANSEN AND MEULENBROEK 21 of 38

The definition of the singular form of the slip gradient and its expansion to obtain the functional form as expressed in Equation C17 form key steps in our formulation. As will be shown below, they allow for a direct definition of the slip-patch end conditions, and a straightforward extension to the double patch configuration.

We note that the numerator in Equation C17 is a power series in z, which we approximate using a (finite) sum of Chebyshev polynomials

$$\frac{d\tilde{\delta}}{dz} = \frac{\sum_{n=0}^{N} c_n T_n(z)}{\sqrt{1 - z^2}},\tag{C19}$$

where $T_n(z)$ are Chebyshev polynomials of the first kind (Mason & Handscomb, 2003).

C1.3. Computation of the Slip

Integration of Equation C19 yields

$$\tilde{\delta}(z) - \tilde{\delta}(1) = \int_{1}^{z} \frac{d\tilde{\delta}}{d\zeta} d\zeta \Rightarrow \tilde{\delta}(z) = \tilde{\delta}(1) + \sum_{n=0}^{N} c_n \int_{1}^{z} \frac{T_n(\zeta)}{\sqrt{1 - \zeta^2}} d\zeta, \tag{C20}$$

which yields (after substitution of $\zeta = \cos \chi$)

$$\tilde{\delta}(z) = \tilde{\delta}(1) + \sum_{n=0}^{N} c_n \int_0^{\arccos z} -\cos(n\chi) d\chi = \sum_{n=0}^{N} c_n \int_0^{\arccos z} -\cos(n\chi) d\chi, \tag{C21}$$

where we made use of the fact that the slip vanishes at the slip patch boundaries, that is, that $\delta(1) = 0$. Performing the integration yields

$$\tilde{\delta}(z) = -c_0 \arccos(z) - \sum_{n=1}^{N} c_n \frac{\sin n \arccos z}{n}.$$
 (C22)

Furthermore, we can write, using the equality $z = \cos \chi$,

$$\sin n \arccos z = \sin \chi \frac{\sin n\chi}{\sin \chi} = \sqrt{1 - z^2} \ U_{n-1}(z), \tag{C23}$$

where $U_n(z)$ are Chebyshev polynomials of the second kind (Mason & Handscomb, 2003), with which we obtain

$$\tilde{\delta}(z) = -c_0 \arccos(z) - \sum_{n=1}^{N} c_n \frac{1}{n} \sqrt{1 - z^2} \ U_{n-1}(z).$$
 (C24)

C1.4. Finite Slip Gradient at the Boundaries

In order to have a finite slip gradient at the boundaries we need to satisfy conditions (C18); these can be translated into conditions on the coefficients c_n by making use of the functional form of the slip gradient introduced in Section (C.1.2). Multiplication of Equation C17 by $\sqrt{1-z^2}$ yields

$$\sqrt{1-z^2} \frac{d\tilde{\delta}}{dz} = r_0 + r_1 z + (1-z^2)(b_0 + b_1 z + \dots).$$
 (C25)

Taking $z \rightarrow \pm 1$ yields

$$\lim_{z \to \pm 1} \left(\sqrt{1 - z^2} \frac{d\tilde{\delta}}{dz} \right) = r_0 \pm r_1, \tag{C26}$$

JANSEN AND MEULENBROEK 22 of 38

which means that we find

$$r_0 = \frac{1}{2} \left[\lim_{z \to 1} \left(\sqrt{1 - z^2} \frac{d\tilde{\delta}}{dz} \right) + \lim_{z \to -1} \left(\sqrt{1 - z^2} \frac{d\tilde{\delta}}{dz} \right) \right], \tag{C27}$$

$$r_1 = \frac{1}{2} \left[\lim_{z \to 1} \left(\sqrt{1 - z^2} \frac{d\tilde{\delta}}{dz} \right) - \lim_{z \to -1} \left(\sqrt{1 - z^2} \frac{d\tilde{\delta}}{dz} \right) \right]. \tag{C28}$$

Using Equation C19 and noting that

$$T_n(1) = \cos 0 = 1,$$
 (C29)

$$T_n(-1) = \cos n\pi = (-1)^n,$$
 (C30)

we have

$$\lim_{z \to 1} \left(\sqrt{1 - z^2} \frac{d\tilde{\delta}}{dz} \right) = \sum_{n=0}^{N} c_n, \tag{C31}$$

$$\lim_{z \to -1} \left(\sqrt{1 - z^2} \frac{d\tilde{\delta}}{dz} \right) = \sum_{n=0}^{N} (-1)^n c_n.$$
 (C32)

This means that our conditions for a finite slip gradient read

$$r_0 = \frac{1}{2} \sum_{n=0}^{N} [1 + (-1)^n] c_n = 0,$$
 (C33)

$$r_1 = \frac{1}{2} \sum_{n=0}^{N} [1 - (-1)^n] c_n = 0.$$
 (C34)

Or, equivalently, both the sum of the even coefficients and the sum of the odd coefficients need to be zero, which can be expressed as (for N even)

$$r_0 = \sum_{n=1}^{N/2} c_{2n} = 0, (C35)$$

$$r_1 = \sum_{n=1}^{N/2} c_{2n-1} = 0. (C36)$$

We note that this result was also obtained by Uenishi and Rice (2003), although via a considerably more complex route, involving an expansion in eigenfunctions, which doesn't allow for a straightforward extension to multiple slip patches.

C1.5. Zero Net Displacement Over the Slip Patch

In addition to the endpoint conditions (C33) and (C34), which correspond to conditions (B7), we also need to fulfill condition (B8) for net zero slip over the slip patch. With the aid of Equation C24 we obtain the simple result

$$\tilde{\delta}(-1) = 0 \Rightarrow c_0 = 0,\tag{C37}$$

such that we end up with

JANSEN AND MEULENBROEK 23 of 38

$$\tilde{\delta}(z) = -\sum_{n=1}^{N} c_n \frac{1}{n} \sqrt{1 - z^2} \ U_{n-1}(z). \tag{C38}$$

We note that this expansion for $\tilde{\delta}$ closely resembles the one used by Uenishi and Rice (2003), who expanded $\tilde{\delta}$ directly in terms of $\sqrt{1-z^2}$ $U_{n-1}(z)$ (i.e., without the term $\frac{1}{n}$), but is different from the one used by Jansen and Meulenbroek (2022) who expanded the scaled pre-slip Coulomb stress in terms of T_n , resulting in a more complex expression for $\tilde{\delta}$.

C1.6. Determining c_n

We can now return to the scaled governing Equation C12 to compute the expansion coefficient c_n . With the aid of Equation C19 and our knowledge that $c_0 = 0$, we obtain for the RHS:

RHS =
$$-\int_{-1}^{1} \frac{\sum_{n=0}^{N} c_n T_n(\zeta)}{\sqrt{1-\zeta^2}} d\zeta = -\sum_{n=1}^{N} c_n \int_{-1}^{1} \frac{T_n(\zeta)}{\sqrt{1-\zeta^2}} d\zeta.$$
 (C39)

We use equation (9.22a) from Mason and Handscomb (2003) to evaluate the integral:

$$\int_{-1}^{1} \frac{T_n(\zeta)}{\sqrt{1-\zeta^2}} dy = \pi U_{n-1}(z).$$
 (C40)

If we combine Equations C39 and C40, and use Equation C38 to rewrite $\tilde{\delta}$ at the LHS, Equation C12 becomes

$$\tilde{r}(z) - \tilde{w}(z) \sum_{n=1}^{N} c_n \frac{1}{n} \sqrt{1 - z^2} \ U_{n-1}(z) = -\pi \sum_{n=1}^{N} c_n U_{n-1}(z).$$
 (C41)

Equation C41 is a linear system of equations for the unknown coefficients c_n in terms of a continuous spatial variable z. "Forward" computation of the induced fault slip δ for a given pressure p can now be performed by using a space-discretized form of Equation C41 in combination with discretized Chebyshev polynomials, as worked out in detail in Section S.1 of the Supporting Information S1. The determination of the slip patch boundaries \tilde{y}_- and \tilde{y}_+ , for a given pressure p, has to be guided by an optimization routine with the objective to reduce the residuals r_0 and r_1 to below a user-defined tolerance. In theory, the number of Chebyshev polynomials N may be increased until a characteristic measure for the solution (e.g., the slip patch length $\tilde{y}_+ - \tilde{y}_-$) achieves a (near-)stationary value, although in practice it may be more convenient to work with a predefined number. The numerical workflow to compute δ starting from a given value of p is given in Algorithm S.1 of the Supporting Information S1. This workflow is valid as long as p remains below the nucleation pressure p^* , the computation of which will be addressed in Appendix D.

C2. Double Slip Patch

For the coupled doublepatch problem we can apply a similar approach. There are two differences; we need to solve Equation 10 in the body of the paper again, but it now has to hold both for $y \in L_1$ and $y \in L_2$. Furthermore the integral at the RHS is now taken over both L_1 and L_2 , where, for $y \in L_1$, the integral over L_2 expresses the effect of the coupling between both patches, and vice versa.

C2.1. Scaling

Using a similar method as for the single patch, we first introduce scaled coordinates

$$\underline{y}_1 = \frac{\tilde{y}_2 - \tilde{y}_1}{2}, \ \ \bar{y}_1 = \frac{\tilde{y}_1 + \tilde{y}_2}{2}, \ \ \underline{y}_2 = \frac{\tilde{y}_4 - \tilde{y}_3}{2} \ \text{and} \ \ \bar{y}_2 = \frac{\tilde{y}_3 + \tilde{y}_4}{2},$$
 (C42)

and the scaled variables, with i = 1, 2,

JANSEN AND MEULENBROEK 24 of 38

$$z_i\left(y;\underline{y}_i,\bar{y}_i\right) = \frac{y - \bar{y}_i}{\underline{y}_i} \Rightarrow y = \underline{y}_i z_i + \bar{y}_i, \tag{C43}$$

$$\zeta_i\left(\xi;\underline{y}_i,\bar{y}_i\right) = \frac{\xi - \bar{y}_i}{y_i} \Rightarrow \xi = \underline{y}_i\zeta_i + \bar{y}_i. \tag{C44}$$

Note that with this scaling we map only one of the patches to the interval [-1,1], whereas the other patch is then outside. Due to the functional form of the inversion formula B5 we have (similar to the single patch problem)

$$\frac{d\delta}{dy} = \frac{h_1(y)}{\sqrt{-(y - \tilde{y}_1)(y - \tilde{y}_2)}} \text{ if } y \in L_1 \text{ and } \frac{d\delta}{dy} = \frac{h_2(y)}{\sqrt{-(y - \tilde{y}_3)(y - \tilde{y}_4)}} \text{ if } y \in L_2,$$
 (C45)

where the remaining terms in the square root expression $\Psi_{\pm}(y)$ are absorbed in functions $h_1(y)$ and $h_2(y)$. We also define

$$\tilde{\delta}_i \left(z_i; p, \underline{y}_i, \bar{y}_i \right) = \frac{\delta \left(y = y \left(z_i; \underline{y}_i, \bar{y}_i \right), p \right)}{y_i} \text{ if } y \in L_i.$$
 (C46)

Using the functional form (C45) and arguing along the same lines as for the single-patch case, we then find

$$\frac{d\tilde{\delta}_1}{dz_1} = \frac{\sum_{n=0}^{N} a_n T_n(z_1)}{\sqrt{1 - z_1^2}} \text{ if } y \in L_1,$$
(C47)

and

$$\frac{d\tilde{\delta}_2}{dz_2} = \frac{\sum_{n=0}^{N} b_n T_n(z_2)}{\sqrt{1 - z_2^2}} \text{ if } y \in L_2.$$
 (C48)

In order to have net zero displacement over both patches, we need to impose

$$a_0 = b_0 = 0,$$
 (C49)

and in order to have finite derivatives at the four boundary points we need

$$r_0 = \frac{1}{2} \sum_{n=0}^{N} [1 + (-1)^n] a_n = 0,$$
 (C50)

$$r_1 = \frac{1}{2} \sum_{n=0}^{N} [1 - (-1)^n] a_n = 0,$$
 (C51)

$$r_2 = \frac{1}{2} \sum_{n=0}^{N} [1 + (-1)^n] b_n = 0,$$
 (C52)

$$r_3 = \frac{1}{2} \sum_{n=0}^{N} [1 - (-1)^n] b_n = 0.$$
 (C53)

We thus obtained the four end conditions for the double-patch case as a natural extension of the single-patch case.

C2.2. Determining a_n and b_n

The Case $y \in L_1$

First we choose $y \in L_1$ and scale

$$\tilde{w}_1\left(z_1; p, \underline{y}_1, \bar{y}_1\right) = \frac{W\left(y = y\left(z_1; \underline{y}_1, \bar{y}_1\right), p\right) \cdot \underline{y}_1}{A},\tag{C54}$$

$$\tilde{r}_1\left(z_1; p, \underline{y}_1, \bar{y}_1\right) = \frac{R\left(y = y\left(z_1; \underline{y}_1, \bar{y}_1\right), p\right)}{A}.$$
(C55)

Furthermore we can use the same procedure as in the single patch case to compute the net displacement

$$\tilde{\delta}_{1}(z_{1}) = -\sum_{n=1}^{N} a_{n} \frac{1}{n} \sqrt{1 - z_{1}^{2}} U_{n-1}(z_{1}), \tag{C56}$$

which means that scaling the LHS of Equation 10 yields

LHS =
$$\tilde{r}_1(z_1) - \tilde{w}_1(z_1) \sum_{n=1}^{N} a_n \frac{1}{n} \sqrt{1 - z_1^2} U_{n-1}(z_1)$$
. (C57)

Scaling the RHS leads to contributions of two terms:

$$-\int_{-1}^{1} \frac{\frac{d\tilde{\delta}}{d\zeta_{1}}(\zeta_{1})}{\zeta_{1} - z_{1}} d\zeta_{1} = -\sum_{n=1}^{N} a_{n} \int_{-1}^{1} \frac{T_{n}(\zeta_{1})}{\sqrt{1 - \zeta_{1}^{2}(\zeta_{1} - z_{1})}} d\zeta_{1} = -\pi \sum_{n=1}^{N} a_{n} U_{n-1}(z_{1}), \tag{C58}$$

and

$$-\int_{-1}^{1} \frac{\frac{d\tilde{\delta}_{2}}{dz_{2}}(z_{2})}{\underline{y}_{2}z_{2} + \bar{y}_{2} - \underline{y}_{1}z_{1} - \bar{y}_{1}} \underline{y}_{2} dz_{2} = -\sum_{n=1}^{N} b_{n} \int_{-1}^{1} \frac{T_{n}(z_{2})}{\sqrt{1 - z_{2}^{2}}(z_{2} - z_{1}\underline{r} + \bar{r})} dz_{2}.$$
 (C59)

where

$$\underline{r} = \frac{y_1}{y_2} \text{ and } \bar{r} = \frac{\bar{y}_2 - \bar{y}_1}{y_2},$$
 (C60)

which represent the relative (projected) patch length and the scaled distance between the (projected) patch centers respectively; see Figure C1.

Note that the integrals in Equation C59 are not singular because the variables z_1 and z_2 in the denominators are defined on different slip patches. Combining Equations C57, C58 and C59 results in:

$$\tilde{r}_{1}(z_{1}) - \tilde{w}_{1}(z_{1}) \sum_{n=1}^{N} a_{n} \frac{1}{n} \sqrt{1 - z_{1}^{2}} U_{n-1}(z_{1})$$

$$= -\pi \sum_{n=1}^{N} a_{n} U_{n-1}(z_{1}) - \sum_{n=1}^{N} b_{n} \int_{-1}^{1} \frac{T_{n}(z_{2})}{\sqrt{1 - z_{2}^{2}} (z_{2} - z_{1}\underline{r} + \overline{r})} dz_{2}.$$
(C61)

The Case $y \in L_2$

Next we choose $y \in L_2$ and scale

JANSEN AND MEULENBROEK 26 of 38

21699356, 2025, 10, Downloaded from https://agupubs.onlinelibrary.wiley.com/doi/10.1029/2025JB031577 by Technical University Delft, Wiley Online Library on [30/10/2025]

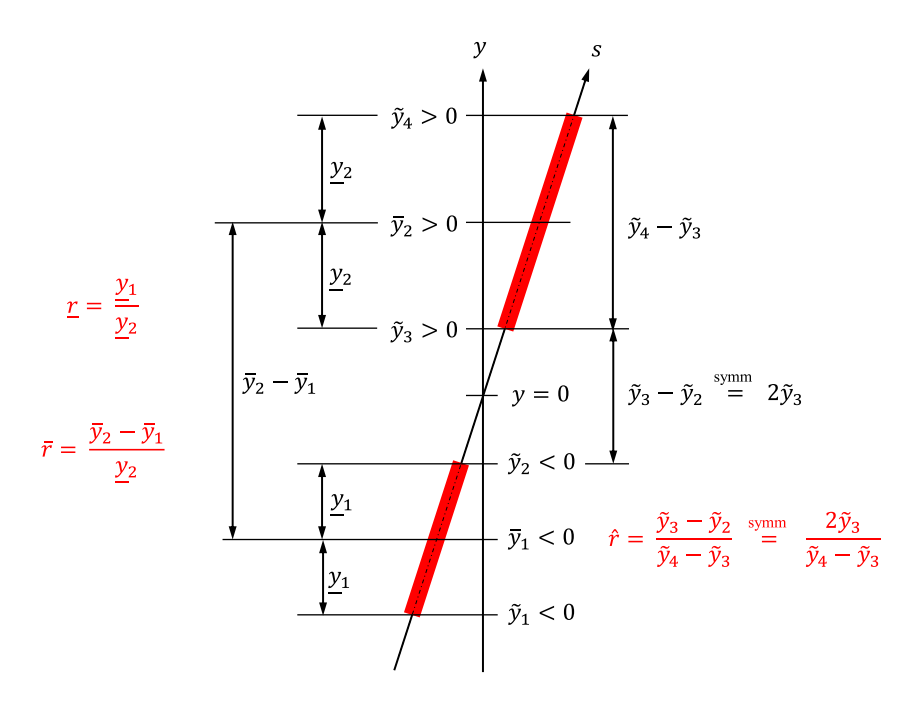


Figure C1. Illustration of geometrical variables and dimensionless parameters (in red font) used in the paper. The two red bars represent the slip patches.

$$\tilde{w}_2\left(z_2; p, \underline{y}_2, \bar{y}_2\right) = \frac{W\left(y = y\left(z_2; \underline{y}_2, \bar{y}_2\right), p\right) \cdot \underline{y}_2}{A},\tag{C62}$$

$$\tilde{r}_2\left(z_2; p, \underline{y}_2, \bar{y}_2\right) = \frac{R\left(y = y\left(z_2; \underline{y}_2, \bar{y}_2\right), p\right)}{A}.$$
(C63)

We can compute the net displacement

$$\tilde{\delta}_2(z_2) = -\sum_{n=1}^{N} b_n \frac{1}{n} \sqrt{1 - z_2^2} U_{n-1}(z_2), \tag{C64}$$

and use the same procedure as in the single patch case to find:

$$\tilde{r}_{2}(z_{2}) - \tilde{w}_{2}(z_{2}) \sum_{n=1}^{N} b_{n} \frac{1}{n} \sqrt{1 - z_{2}^{2}} U_{n-1}(z_{2})$$

$$= -\pi \sum_{n=1}^{N} b_{n} U_{n-1}(z_{2}) - \sum_{n=1}^{N} a_{n} \int_{-1}^{1} \frac{T_{n}(z_{1})}{\sqrt{1 - z_{1}^{2}} \left(z_{1} - \frac{z_{2}}{r} - \frac{\bar{r}}{r}\right)} dz_{1}.$$
(C65)

C2.3. Integration of the Cross Terms

The last terms at the RHSs of Equations C61 and C65 can be integrated analytically with the aid of contour integration; see Section (D.3). However, this does not lead to a computational advantage in comparison to (regular) Gauss-Chebyshev quadrature and we therefore revert to the latter with the aid of Equations B10 and B12. For the integral in Equation C61 this leads to

$$\int_{-1}^{1} \frac{T_n(z_2)}{\sqrt{1 - z_2^2} (z_2 - z_1 \underline{r} + \overline{r})} dz_2 \approx \sum_{m=1}^{M} \frac{\pi}{M} \frac{T_n(z_m)}{z_m - z_1 \underline{r} + \overline{r}}.$$
 (C66)

JANSEN AND MEULENBROEK 27 of 38

A similar expression is obtained for the integral in Equation C65 by substituting z_2 for z_1 , $\frac{1}{r}$ for \underline{r} , and $-\frac{\bar{r}}{r}$ for \bar{r} in the RHS of Equation C66.

C2.4. The Combined Equation

Equations C61 and C65 jointly form a linear system of equations for the coefficients a_n and b_n . A representation in terms of discretized Chebyshev polynomials, while using Gauss-Chebyshev quadrature for the cross terms, is given in Section S.2 of the Supporting Information S1. The numerical workflow to compute δ in both slip patches starting from a given value of p is now equivalent to the single-patch case; see Algorithm S.2 in Supporting Information S1.

Appendix D: Eigenproblem

D1. Single Slip Patch

D1.1. Discrete Formulation

The scaled version of eigenproblem (12) can be written as

$$\tilde{w}(z,p)\dot{\tilde{\delta}}(z,p) = -\int_{L(p)} \frac{d\dot{\tilde{\delta}}}{\zeta}(\zeta,p) \frac{d\zeta}{\zeta - z} d\zeta, \tag{D1}$$

where we note that p has not been scaled and still has dimension "pressure," but that this has no consequences for the subsequent analysis. In analogy to Equation C38, the slip rate can be expanded as

$$\dot{\tilde{\delta}}(z) = -\sum_{n=1}^{N} e_n \frac{1}{n} \sqrt{1 - z^2} \ U_{n-1}(z), \tag{D2}$$

and with the aid of the derivation leading to Equation C41, Equation D1 can be expressed in a similar fashion as

$$\tilde{w}(z) \sum_{n=1}^{N} e_n \frac{1}{n} \sqrt{1 - z^2} \ U_{n-1}(z) = \pi \sum_{n=1}^{N} e_n U_{n-1}(z).$$
 (D3)

Equation D3 represents a (generalized) eigenproblem. We can benefit from the orthogonality properties of the Chebyshev polynomials by multiplying the equation with $\sqrt{1-z^2} U_{m-1}(z)$ and integrating from -1 to 1 which yields

$$\pi \cdot \frac{\pi}{2} \sum_{n=1}^{M} \delta_{mn} e_n = \frac{\pi^2}{2} e_m = \sum_{n=1}^{N} \frac{1}{n} \alpha_{mn} e_n, \tag{D4}$$

where

$$\alpha_{mn} = \int_{-1}^{1} \sqrt{1 - z^2} \, U_{m-1}(z) \, \tilde{w}(z) \sqrt{1 - z^2} \, U_{n-1}(z) \, dz. \tag{D5}$$

For the general case where \tilde{w} is a function of z, we cannot find explicit expressions for the terms α_{mn} . (For the specific case where \tilde{w} is a constant, we can find explicit expressions, but they are not particularly elegant). We therefore use (regular) Gauss-Chebyshev quadrature to obtain, see Equations B11 and B13,

$$\alpha_{mn} = \sum_{p=1}^{N} \pi \frac{1 - z_p^2}{N+1} U_{m-1}(z_p) \tilde{w}(z_p) \sqrt{1 - z_p^2} U_{n-1}(z_p).$$
 (D6)

JANSEN AND MEULENBROEK 28 of 38

Combining Equations D4 to D6, and expressing the result in discretized form results in

$$(\mathbf{B} - \lambda_i \mathbf{I}) \, \mathbf{e}_i = \mathbf{0},\tag{D7}$$

where we introduced the (scaled) eigenvalues λ_i and eigenvectors \mathbf{e}_i for i = 1, ..., N, and where matrix \mathbf{B} is defined in detail in Section S.3 of the Supporting Information S1 while \mathbf{I} is the unit matrix.

D1.2. Non-Uniform Slip Weakening-Single Patch

In our application, \tilde{w} is a function of z, while, moreover, it is a function p. The values of λ_i in Equation D7 are therefore also dependent on p. They represent the inverse of the scaled slip patch length Δz_{eig} defined as

$$\Delta z_{eig}(p) = \frac{\Delta y_{eig}(p)}{2y(p)},\tag{D8}$$

which means that we have

$$\Delta y_{eig}(p) = 2\underline{y}(p)\Delta z_{eig}(p) = \frac{2\underline{y}(p)}{\lambda_{\max}(p)}.$$
 (D9)

Nucleation occurs when $p = p^*$, where p^* is the pressure at which the simulated nucleation length

$$\Delta y_{sim}(p) = 2 y_{sim}(p) = \tilde{y}_{+}(p) - \tilde{y}_{-}(p)$$
 (D10)

just equals the eigenvalue-related length $\Delta y_{eig}(p)$, that is, nucleation occurs when $\lambda_{\max}(p) = 1$. The corresponding value $\Delta y_{sim}^*(p^*) = \Delta y_{eig}^*(p^*)$ is then the true nucleation length.

D1.3. Uniform Slip Weakening-Single Patch

Uenishi and Rice (2003) considered a situation in which \tilde{w} is a constant, and therefore independent of z and p. In that case, we can isolate \tilde{w} from Equation D6 and formulate a modified version of Equation D7 as

$$(\widetilde{\mathbf{B}} - \widetilde{\lambda}_i \mathbf{I})\widetilde{\mathbf{e}}_i = \mathbf{0},\tag{D11}$$

where matrix $\widetilde{\mathbf{B}}$ is given in detail in Section S.3 of the Supporting Information S1, and where the eigenvalues $\widetilde{\lambda}_i$ now incorporate \widetilde{w} . (Note that λ_i and $\widetilde{\lambda}_i$ are therefore differently scaled.) The largest eigenvalue $\widetilde{\lambda}_{\max}$ can be expressed as

$$\tilde{\lambda}_{\text{max}} = \frac{\pi}{\tilde{w}} = \frac{\pi A}{W_{\text{V}}},\tag{D12}$$

and because the patch length can be written as

$$\Delta y = \tilde{y}_+ - \tilde{y}_- = 2y,\tag{D13}$$

the nucleation length follows from Equation D12 as

$$\Delta y_{eig}^* = 2\underline{y} = \frac{1}{\tilde{\lambda}_{max}} \frac{2\pi A}{W} = \frac{1}{\tilde{\lambda}_{max}} \frac{G}{W(1-\nu)} \approx \Delta y_{U\&R}^* = 1.158 \frac{G}{W(1-\nu)}, \tag{D14}$$

where $\tilde{\lambda}_{max}$ can be obtained by numerically solving Equation D11, and where the approximation corresponds to taking into account a finite number of Chebyshev polynomials. The number 1.158 is the value for $\tilde{\lambda}_{max}^{-1}$ as obtained by Uenishi and Rice (2003) using 5 polynomials. With 100 polynomials, Dascalu et al. (2000) obtained

 $\tilde{\lambda}_{\text{max}}^{-1} = 1.15777388$, while with $2^{11} = 2048$ polynomials we find $\tilde{\lambda}_{\text{max}}^{-1} = 1.157773883697589$; see Section D.2.5 for a convergence analysis. For practical applications, the short number 1.158 suffices.

We note that Uenishi and Rice (2003) also obtained a closed-form expression for the nucleation pressure p^* , based on the eigenvector corresponding to $\tilde{\lambda}_{max}$, but this feature depends on their particular choice of the pre-slip Coulomb stress and does not seem to allow for an extension to the more complex stress distribution in our application of interest.

D1.4. Small Effect of Non-Uniform Slip Weakening-Single Patch

As proposed by Van den Bogert (2018) and Buijze et al. (2019), the U&R solution (D14) can be "stretched" for use with a spatially varying and pressure-dependent W(y,p) according to

$$\Delta y_{eig}(p) \approx \Delta y_{U\&R}(p) = 1.158 \frac{G}{\overline{W}(p)(1-\nu)},$$
(D15)

where \overline{W} is an averaged value over the slip patch:

$$\overline{W}(p) = \frac{1}{\tilde{y}_{+}(p) - \tilde{y}_{-}(p)} \int_{\tilde{y}_{-}(p)}^{\tilde{y}_{+}(p)} W(y, p) \, dy. \tag{D16}$$

Because $\Delta y_{U\&R}(p)$ now depends on $\tilde{y}_{-}(p)$ and $\tilde{y}_{+}(p)$, which are also changing with p, use of Equation D15 requires a search strategy that involves varying p to find the nucleation length $\Delta y_{U\&R}^*(p^*)$, as discussed in more detail in the body of the text.

D2. Double Slip Patch

D2.1. Non-Uniform Slip Weakening-Double Patch

Using the same reasoning as for the single-patch case, the double-patch version of the eigenproblem with spatially varying parameters $\tilde{w}_1(z)$ and $\tilde{w}_2(z)$ can be expressed as

$$\tilde{w}_{1}(z_{1}) \sum_{n=1}^{N} e_{1,n} \frac{1}{n} \sqrt{1 - z_{1}^{2}} \ U_{n-1}(z_{1}) = \pi \sum_{n=1}^{N} e_{1,n} U_{n-1}(z_{1})$$

$$+ \sum_{n=1}^{N} e_{2,n} \int_{-1}^{1} \frac{T_{n}(z_{2})}{\sqrt{1 - z_{2}^{2}} (z_{2} - z_{1}\underline{r} + \overline{r})} dz_{2},$$
(D17)

$$\tilde{w}_{2}(z_{2}) \sum_{n=1}^{N} e_{2,n} \frac{1}{n} \sqrt{1 - z_{2}^{2}} U_{n-1}(z_{2}) = \pi \sum_{n=1}^{N} e_{2,n} U_{n-1}(z_{2})$$

$$+ \sum_{n=1}^{N} e_{1,n} \int_{-1}^{1} \frac{T_{n}(z_{1})}{\sqrt{1 - z_{1}^{2}} \left(z_{1} - \frac{z_{2}}{r} - \frac{\bar{r}}{r}\right)} dz_{1},$$
(D18)

which can be represented in discretized form as

$$\begin{pmatrix}
\begin{bmatrix} \mathbf{B}_{11} & \mathbf{B}_{12} \\ \mathbf{B}_{21} & \mathbf{B}_{22} \end{bmatrix} - \lambda_i \begin{bmatrix} \mathbf{I} & \boldsymbol{\theta} \\ \boldsymbol{\theta} & \mathbf{I} \end{bmatrix} \end{pmatrix} \begin{bmatrix} \mathbf{e}_1 \\ \mathbf{e}_2 \end{bmatrix}_i = \begin{bmatrix} \boldsymbol{\theta} \\ \boldsymbol{\theta} \end{bmatrix},$$
(D19)

with details of submatrices \mathbf{B}_{jk} given in Section S.4 of the Supporting Information S1. Note that the integrals in Equations D17 and D18, representing cross terms, are not singular because z_1 and z_2 are defined on different slip patches. The pressure-dependent value for each of the slip patch lengths is now given by

JANSEN AND MEULENBROEK 30 of 38

$$\Delta y_{eig,j}(p) = 2 \underbrace{y_j}(p) \Delta z_{eig,j}(p) = \frac{2 \underbrace{y_j}(p)}{\lambda_{\max}(p)} = \frac{\tilde{y}_{(2j-1)}(p) - \tilde{y}_{(2j)}(p)}{\lambda_{\max}(p)}, \quad j = 1, 2.$$
 (D20)

Nucleation occurs when the simulated slip patch length $\Delta y_{sim,j}(p)$ becomes just equal to $\Delta y_{eig,j}(p)$, that is, when $\lambda_{\max}(p)$ becomes equal to one in at least one of the patches.

D2.2. Uniform Slip Weakening-Double Patch

D2.2.1. Parameter Dependence

Unlike in the single-patch case, in the double-patch case we cannot isolate parameters \tilde{w}_1 and \tilde{w}_2 by dividing them out from Equations D17 and D18; see also the block structure of matrix **B** in Section S.4 of the Supporting Information S1 which has the parameters appearing in the diagonal blocks but not in the off-diagonal ones. Therefore, an expression for the nucleation length will have the form:

$$\Delta y_{eig,j} = \frac{2\pi A}{\hat{\lambda}_{\max}(\tilde{w}_1, \tilde{w}_2, \bar{r})} = \frac{G}{\hat{\lambda}_{\max}(\tilde{w}_1, \tilde{w}_2, \bar{r}) \cdot (1 - \nu)} = f(\tilde{w}_1, \tilde{w}_2, \bar{r}) \cdot \frac{G}{(1 - \nu)}, \quad j = 1, 2.$$
 (D21)

where \bar{r} was defined in Equation C60. (Note that λ_i , $\tilde{\lambda}_i$ en $\hat{\lambda}_i$ are all differently scaled.) The value of $f(\tilde{w}_1, \tilde{w}_2, \bar{r})$ follows on a case-by-case basis from solving eigenproblem (D19), making it impossible to find a simple result as in the original U&R formulation (D14).

D2.2.2. Symmetric Case

As discussed in the body of the text, in a symmetric situation $\underline{r}=1$ and we have only a single parameter \tilde{w} . Moreover, the cross terms are absent such that we can divide out \tilde{w} again. This implies that f, and thus λ_{\max} , becomes a function of only one additional parameter: $f(\bar{r}) = (\hat{\lambda}_{\max}(\bar{r}))^{-1}$. We will therefore formulate the corresponding eigenproblem for the symmetric case.

For the double-patch configuration we obtain symmetric slip patches with $\tilde{y}_1 = -\tilde{y}_4$ and $\tilde{y}_2 = -\tilde{y}_3$. Equation 12 then becomes

$$W\dot{\delta}(y) = -A \left(\int_{\tilde{y}_{1}}^{\tilde{y}_{2}} \frac{\nabla \dot{\delta}(\xi)}{\xi - y} d\xi + \int_{\tilde{y}_{3}}^{\tilde{y}_{4}} \frac{\nabla \dot{\delta}(\xi)}{\xi - y} d\xi \right)$$

$$= -A \left(\int_{-\tilde{y}_{4}}^{-\tilde{y}_{3}} \frac{\nabla \dot{\delta}(\xi)}{\xi - y} d\xi + \int_{\tilde{y}_{3}}^{\tilde{y}_{4}} \frac{\nabla \dot{\delta}(\xi)}{\xi - y} d\xi \right)$$

$$= -A \int_{\tilde{y}_{3}}^{\tilde{y}_{4}} \frac{2\xi \nabla \dot{\delta}(\xi)}{\xi^{2} - y^{2}} d\xi,$$

$$= -A \int_{\tilde{y}_{5}}^{\tilde{y}_{4}} \frac{\nabla \dot{\delta}(\xi)}{\xi - y} \frac{2\xi}{\xi + y} d\xi,$$
(D22)

where we dropped the dependence on p from the notation.

Scaling the equation, using Equations C1 to C3, C8 C9 and C60, results in

$$\tilde{w}\,\dot{\tilde{\delta}}(z) = -\int_{-1}^{1} \frac{\frac{d\tilde{\delta}}{dz}(\zeta)}{(\zeta - z)} \frac{2\zeta + \bar{r}}{(\zeta + z + \bar{r})} d\zeta,\tag{D23}$$

where \bar{r} now reduces to

JANSEN AND MEULENBROEK 31 of 38

$$\bar{r} = \text{symm} \frac{2\bar{y}_2}{y_2} = \frac{2(\tilde{y}_3 + \tilde{y}_4)}{\tilde{y}_4 - \tilde{y}_3}.$$
 (D24)

In analogy to Equations C19 and C38 this can be rewritten as

$$\tilde{w} \sum_{n=1}^{N} e_n \frac{1}{n} \sqrt{1 - z^2} \ U_{n-1}(z) = \sum_{n=1}^{N} e_n \int_{-1}^{1} \frac{T_n(\zeta)}{\sqrt{1 - \zeta^2} (\zeta - z)} \frac{2\zeta + \bar{r}}{(\zeta + z + \bar{r})} d\zeta. \tag{D25}$$

Discretizing the spatial variable z with second-kind Chebyshev points $z_p, p = 1, ..., N$, as defined in Equation B13, we obtain

$$\tilde{w} \sum_{n=1}^{N} e_n \frac{1}{n} \sqrt{1 - z_p^2} \ U_{n-1}(z_p) = \sum_{n=1}^{N} e_n \int_{-1}^{1} \frac{T_n(\zeta)}{\sqrt{1 - \zeta^2} (\zeta - z_p)} \frac{2\zeta + \bar{r}}{(\zeta + z_p + \bar{r})} d\zeta.$$
 (D26)

D2.2.3. Analytical Solution

As shown in detail in Section D.3, the integral in Equation D25 can be expressed as

$$\int_{-1}^{1} \frac{T_n(\zeta)}{\zeta - z} \frac{1}{\sqrt{1 - \zeta^2}} \frac{2\zeta + \bar{r}}{\zeta + z + \bar{r}} d\zeta = \pi U_{n-1}(z) + \pi \frac{\omega_+^n}{\sqrt{\alpha^2 - 1}},$$
(D27)

where

$$\alpha = \bar{r} + z > 1, \ \omega_{+} = -\alpha + \sqrt{\alpha^{2} - 1} < 0,$$
 (D28)

such that ω_+ depends on z and \bar{r} via $\alpha = \bar{r} + z$. Equation D26 thus becomes

$$\tilde{w} \sum_{n=1}^{N} e_n \frac{1}{n} \sqrt{1 - z_p^2} \ U_{n-1}(z_p) = \sum_{n=1}^{N} e_n \left(\pi U_{n-1}(z_p) + \pi \frac{\omega_{p+}^n}{\sqrt{\alpha_p^2 - 1}} \right), \tag{D29}$$

where α_p and ω_{p+} are discretized versions of α and ω_+ .

Following the development in Section D.1, we define the eigenproblem

$$(\hat{\mathbf{B}} - \hat{\lambda}_i \mathbf{I}) \,\hat{\mathbf{e}}_i = \mathbf{0},\tag{D30}$$

where $\hat{\mathbf{B}}$ is specified in detail again in Section S.4 of the Supporting Information S1, and where $\hat{\lambda}_{max}$ can be expressed as

$$\hat{\lambda}_{\text{max}} = \frac{\pi}{\tilde{w}} = \frac{\pi A}{Wy}.$$
 (D31)

An EU&R expression for the nucleation length in a symmetric case with coupling between the slip patches now becomes

$$\Delta y_{EU\&R}^* = \frac{2\pi A}{W\hat{\lambda}_{\max}(\bar{r})} = \frac{G}{W(1-\nu)\hat{\lambda}_{\max}(\bar{r})} = f(\bar{r}) \frac{G}{W(1-\nu)},\tag{D32}$$

with a value of $f(\bar{r}) = (\hat{\lambda}_{\max}(\bar{r}))^{-1}$ that follows from solving eigenproblem (D30).

JANSEN AND MEULENBROEK 32 of 38

D2.2.4. Gauss-Chebyshev Quadrature

Alternatively, the integration of the RHS of Equation D26 can be performed with augmented Gauss-Chebyshev quadrature as defined in Equation B14. Note the functional similarity between the second-kind points and the augmented first-kind points defined in Equations B13 and B15 respectively, which we use to express Equation B14 as

$$\int_{-1}^{1} \frac{F(\zeta)}{\sqrt{1-\zeta^{2}}(\zeta-z)} d\zeta \approx \sum_{m=1}^{N+1} \frac{\pi}{N+1} \frac{F(\zeta_{m})}{\zeta_{m}-z_{p}},$$
 (D33)

where

$$\zeta_m = \cos\frac{(m - \frac{1}{2})\pi}{N + 1}, \ m = 1, \dots, N + 1,$$
 (D34)

$$z_p = \cos \frac{p\pi}{N+1}, \ p = 1, \dots, N.$$
 (D35)

Equation D26 can now be written as

$$-\tilde{w}\sum_{n=1}^{N}e_{n}\frac{1}{n}\sqrt{1-z_{p}^{2}}\ U_{n-1}(z_{p}) = -\sum_{n=1}^{N}e_{n}\sum_{m=1}^{N+1}\frac{\pi}{N+1}\frac{T_{n}(\zeta_{m})}{(\zeta_{m}-z_{p})}\frac{2\zeta_{m}+\bar{r}}{(\zeta_{m}+z_{p}+\bar{r})},\tag{D36}$$

which can be expressed in discrete form as specified in Section S.4 of the Supporting Information S1, resulting in a corresponding version of matrix $\hat{\mathbf{B}}$ in eigenproblem (D30).

D2.3. Small Effect of Non-Uniform Slip Weakening-Double Patch

The EU&R solution can be "stretched" for use with a spatially varying and pressure-dependent W(y,p) just like was done for the single-patch U&R solution. Equation D32 should then be written as

$$\Delta y_{eig}(p) \approx \Delta y_{EU\&R}(p) = f(\bar{r}) \frac{G}{\overline{W}(1-\nu)},$$
 (D37)

where \overline{W} is an averaged value over the slip patch:

$$\overline{W}(p) = \frac{1}{\tilde{y}_{+}(p) - \tilde{y}_{-}(p)} \int_{\tilde{y}_{-}(p)}^{\tilde{y}_{+}(p)} W(y, p) \, dy, \tag{D38}$$

with \tilde{y}_{-} and \tilde{y}_{+} representing either \tilde{y}_{1} and \tilde{y}_{2} , or \tilde{y}_{3} and \tilde{y}_{4} depending on whether stability of the bottom patch or the top patch is considered. This "stretched" version of the EU&R criterion is particularly simple to use in combination with the approximation of $f(\bar{r})$ as defined in Equation 18 in the body of the text. Just like for the single-patch case, use of Equation D37 requires a search strategy that involves varying p to find the nucleation length $\Delta y_{EU\&R}^*(p^*)$.

D2.4. Visualization

To visualize the results, we introduce an alternative scaled parameter (see Figure C1)

$$\hat{r} = \frac{\bar{r}}{2} - 1 = \frac{\tilde{y}_3 - \tilde{y}_2}{\tilde{y}_4 - \tilde{y}_3} \stackrel{\text{symm}}{=} \frac{2\tilde{y}_3}{\tilde{y}_4 - \tilde{y}_3}, \quad 0 < \hat{r},$$
 (D39)

which represents the distance between the (projected) symmetric slip patches scaled with the (projected) patch length. Figure 6 in the body of the text depicts the values of $f(\hat{r})$ as a function of \hat{r} for the analytical and numerical results (in blue and orange respectively) in comparison to the value of $f_{\infty} = f(\hat{r} \uparrow \infty) = 1.158$ for the single-patch

JANSEN AND MEULENBROEK 33 of 38

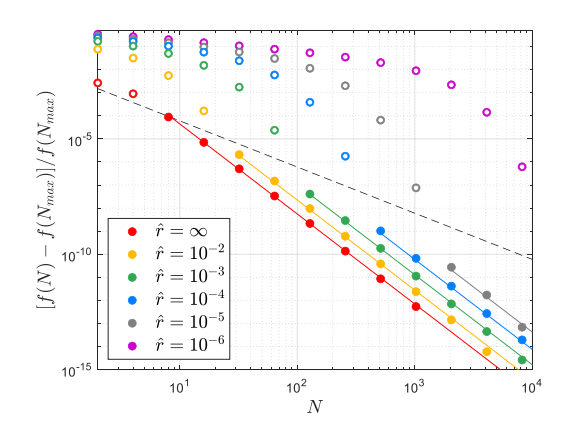


Figure D1. Convergence behavior of the factor $f(\hat{r})$ as a function of the number of Chebyshev polynomials N for decreasing values of the scaled patch distance \hat{r} . The black dashed line represents quadratic convergence $e \sim \frac{1}{N^2}$ where $e = [f(N) - f(N_{\text{max}})]/f(N_{\text{max}})$ is the relative error between f(N) and the most accurate estimate $f(N_{\text{max}})$. Open dots represent results before spectral convergence commences. Solid dots, connected with lines, represent results that converge spectrally with $e \sim \frac{1}{N^{3.9}}$. For $\hat{r} = 10^{-6}$ (purple open dots), spectral convergence is not reached for the maximum number of polynomials $N_{\text{max}} = 2^{14} = 16384$.

case (in red). The numerical and analytical results match exactly, while the numerical approach is computationally somewhat more efficient.

The function $f(\hat{r})$ has been tabulated in an Excel file in Supporting Information S2, and can be approximated with the curve-fitted expression (18) in the body of the text.

D2.5. Convergence

Figure D1 displays the convergence behavior of the factor $f(\hat{r})$ as a function of the number of Chebyshev polynomials N for decreasing values of the scaled patch distance \hat{r} . For all but very small values of \hat{r} , that is, for $10^{-5} < \hat{r} < \infty$, spectral convergence is obtained which implies that the relative error e between f(N) and the most accurate estimate $f(N_{\text{max}})$ decreases faster than quadratically (Boyd, 2001); in this case we observe near-fourth-power convergence. However, for $10^{-5} < \hat{r} < 10^{-1}$, an increasing number of "preconvergent" results (open dots) occurs for decreasing values of \hat{r} , which implies that an increasingly large number of polynomials is required to obtain reliable results. For $\hat{r} = \infty$ (the single-patch case) spectral convergence already starts at $N = 2^3$ and saturates at $N_{\text{max}} = 2^{11}$ (i.e., results for larger values of N are identical.) For $\hat{r} = 10^{-6}$ (almost touching slip patches), convergence cannot be obtained within the memory limits of the software to compute the eigenvalues ($N_{\text{max}} = 2^{14} = 16384$).

D3. Integral in Equation D27

In Equation D27 we used the integral

$$I_{1} = P.V. \int_{-1}^{1} \frac{T_{n}(\zeta)}{\zeta - z} \frac{1}{\sqrt{1 - \zeta^{2}}} \frac{2\zeta + \bar{r}}{\zeta + z + \bar{r}} d\zeta = \pi U_{n-1}(z) + \pi \frac{\omega_{+}^{n}}{\sqrt{\alpha^{2} - 1}},$$
(D40)

where

$$\alpha = \bar{r} + z > 1, \ \omega_+ = -\alpha + \sqrt{\alpha^2 - 1} < 0,$$
 (D41)

such that ω_+ depends on z and \bar{r} via $\alpha = \bar{r} + z$.

Integral I_1 can be derived as follows. We start from the well-know relationship (Abramowitz & Stegun, 1972; Mason & Handscomb, 2003)

$$I_0 = \text{P.V.} \int_{-1}^{1} \frac{T_n(\zeta)}{\zeta - z} \frac{1}{\sqrt{1 - \zeta^2}} d\zeta = \pi U_{n-1}(z).$$
 (D42)

Next, we use

$$\frac{2\zeta + \bar{r}}{\zeta + z + \bar{r}} = \frac{\zeta + \bar{r} + z + \zeta - z}{\zeta + z + \bar{r}},\tag{D43}$$

to write

$$I_{1} = P.V. \int_{-1}^{1} \frac{T_{n}(\zeta)}{\zeta - z} \frac{1}{\sqrt{1 - \zeta^{2}}} \frac{\zeta + \bar{r} + z + \zeta - z}{\zeta + z + \bar{r}} d\zeta = I_{0} + \int_{-1}^{1} \frac{T_{n}(\zeta)}{\sqrt{1 - \zeta^{2}}} \frac{1}{\zeta + z + \bar{r}} d\zeta, \tag{D44}$$

and we define

$$I_2 = \int_{-1}^{1} \frac{T_n(\zeta)}{\sqrt{1 - \zeta^2}} \frac{1}{\zeta + z + \bar{r}} d\zeta, \tag{D45}$$

and use $\zeta = \cos \theta$ to rewrite

$$I_2 = \int_0^{\pi} \frac{\cos n\theta}{\cos \theta + z + \bar{r}} \, d\theta. \tag{D46}$$

Note that I_2 is not singular because $\bar{r} > 2$. We have

$$I_2 = \frac{1}{2} \int_{-\pi}^{\pi} \frac{\cos n\theta}{\cos \theta + z + \bar{r}} d\theta = \frac{1}{2} \int_{-\pi}^{\pi} \frac{\operatorname{Re} e^{in\theta}}{\cos \theta + z + \bar{r}} d\theta = \frac{1}{2} \operatorname{Re} \int_{-\pi}^{\pi} \frac{e^{in\theta}}{\cos \theta + z + \bar{r}} d\theta, \tag{D47}$$

which, setting $\omega = e^{i\theta}$, can be converted in a contour integral along the unit circle:

$$I_2 = \frac{1}{2} \operatorname{Re} \oint_{|\omega| = 1} \frac{\omega^n}{\frac{1}{2}(\omega + \frac{1}{2}) + z + \bar{r}} \frac{-id\omega}{\omega} = \operatorname{Re} \oint_{|\omega| = 1} \frac{-i\omega^n}{\omega^2 + 2\omega(z + \bar{r}) + 1} d\omega. \tag{D48}$$

Note that

$$\omega^2 + 2\omega(z + \bar{r}) + 1 = (\omega - \omega_+)(\omega - \omega_-), \tag{D49}$$

where both $\omega_{\pm} \in \mathbb{R}$ because

$$4(z+\bar{r})^2 - 4 > 0, (D50)$$

since $z + \bar{r} > 1$. Furthermore, we know that

$$\omega_+\omega_- = 1, \tag{D51}$$

which means that either ω_+ or ω_- is inside the unit circle. Solving yields

$$\omega_{\pm} = -\alpha \pm \sqrt{\alpha^2 - 1}, \ \alpha = z + \bar{r}. \tag{D52}$$

Using the Theorem of Residues we find

$$\oint_{|\omega|=1} \frac{-i\omega^n}{\omega^2 + 2\omega(z + \bar{r}) + 1} d\omega = \oint_{|\omega|=1} \frac{-i\omega^n}{(\omega - \omega_+)(\omega - \omega_-)} d\omega = 2\pi i \operatorname{Res}_{\omega = \omega_+} f(\omega), \tag{D53}$$

where

$$f(\omega) = \frac{-i\omega^n}{(\omega - \omega_+)(\omega - \omega_-)},\tag{D54}$$

such that

$$\operatorname{Res}_{\omega = \omega_{+}} f(\omega) = \frac{-i\omega_{+}^{n}}{\omega_{+} - \omega_{-}} = \frac{-i\omega_{+}^{n}}{2\sqrt{\alpha^{2} - 1}},$$
 (D55)

This leads to

JANSEN AND MEULENBROEK 35 of 38

21699356, 2025, 10, Downle

Acknowledgments

This publication is part of the project

"NEPTUNUS: Novel methods for the

the Transient natUre of iNdUced

Research Council (NWO).

Evaluation and Physical understanding of

Seismicity" (with project number DEEP.

NL.2023.020 of the research programme

"DeepNL" which is financed by the Dutch

$$\oint_{|\omega|=1} \frac{-i\omega^n}{\omega^2 + 2\omega(z+\bar{r}) + 1} d\omega = 2\pi i \cdot \frac{-i\omega_+^n}{2\sqrt{\alpha^2 - 1}} = \frac{\pi\omega_+^n}{\sqrt{\alpha^2 - 1}},$$
(D56)

which is already real, which implies that

$$I_2 = \frac{\pi \omega_+^n}{\sqrt{\alpha^2 - 1}}.\tag{D57}$$

We note that the result for I_2 can also be used to solve the cross terms in Equations C61 and C65 analytically. However, because the numerical alternative, in the form of Gauss-Chebyshev formulation, outperforms the analytical solution, we only documented the numerical approach in Subsection C.2.3.

Data Availability Statement

The Matlab code used to produce all figures in this paper is available via the 4TU.ResearchData repository (Jansen & Meulenbroek, 2025).

References

Abramowitz, M., & Stegun, I. (1972). Handbook of mathematical functions with formulas, graphs, and mathematical tables, 10th printing. USA National Bureau of Standards.

Bilby, B., & Eshelby, J. (1968). Dislocations and the theory of fracture. In H. Liebowitz (Ed.), Fracture - An advanced treatise (Vol. 1, pp. 99–182). Academic Press.

Biot, M. (1941). General theory of three-dimensional consolidation. *Journal of Applied Physics*, 12(2), 155–164. https://doi.org/10.1063/1.1712886

Bourne, S. J., Oates, S. J., & Van Elk, J. (2018). The exponential rise of induced seismicity with increasing stress levels in the Groningen gas field and its implications for controlling seismic risk. *Geophysical Journal International*, 213(3), 1693–1700. https://doi.org/10.1093/gji/ggy084 Boyd, J. (2001). In *Chebyshev and fourier spectral methods*, 2nd. Dover.

Brantut, N., & Viesca, R. (2014). Earthquake nucleation in intact or healed rocks. *Journal of Geophysical Research: Solid Earth*, 120(1), 191–209. https://doi.org/10.1002/2014JB011518

Bruhat, L., & Segall, P. (2017). Deformation rates in northern cascadia consistent with slow updip propagation of deep interseismic creep. *Geophysical Journal International*, 211(1), 427–449. https://doi.org/10.1093/gii/ggx317

Buijze, A., Van den Bogert, P., Wassing, B., & Orlic, B. (2019). Nucleation and arrest of dynamic rupture induced by reservoir depletion. *Journal of Geophysical Research: Solid Earth*, 124(4), 3620–3645. https://doi.org/10.1029/2018JB016941

Buijze, A., Van den Bogert, P., Wassing, B., Orlic, B., & Ten Veen, J. (2017). Fault reactivation mechanisms and dynamic rupture modelling of production-induced seismic events in a Rotliegend gas reservoir. *Netherlands Journal of Geosciences*, 96(5), S131–S148. https://doi.org/10.1017/big.2017.27

Buijze, A., Veldkamp, H., & Wassing, B. (2023). Comparison of hydrocarbon and geothermal energy production in the Netherlands: Reservoir characteristics, pressure and temperature changes, and implications for fault reactivation. *Netherlands Journal of Geosciences*, 102, e7. https://doi.org/10.1017/njg.2023.6

Candela, T., Osinga, S., Ampuero, J., Wassing, B., Pluymaekers, M., Fokker, P., et al. (2019). Depletion-induced seismicity at the Groningen gas field: Coulomb rate-and-state models including differential compaction effect. *Journal of Geophysical Research: Solid Earth*, 124(7), 7081–7104. https://doi.org/10.1029/2018JB016670

Cappa, F., & Rutqvist, J. (2011). Impact of CO2 geological sequestration on the nucleation of earthquakes. *Geophysical Research Letters*, 38(17), L17313. https://doi.org/10.1029/2011GL048487

Cornelissen, P., Meulenbroek, B. J., & Jansen, J. D. (2024). On the derivation of closed-form expressions for displacements, strains, and stresses inside poroelastic reservoirs. *Journal of Geophysical Research: Solid Earth*, 129(2), e2023JB027733. https://doi.org/10.1029/2023jb027733

Dascalu, C., Ionescu, I., & Campillo, M. (2000). Fault finiteness and initiation of dynamic shear instability. *Earth and Planetary Science Letters*, 177(3–4), 163–176. https://doi.org/10.1016/S0012-821X(00)00055-8

De Jager, J., & Visser, C. (2017). Geology of the Groningen field – An overview. Netherlands Journal of Geosciences, 96(5), s3–s15. https://doi.org/10.1017/njg.2017.22

Dempsey, D., & Suckale, J. (2023). Physics-based forecasting of induced seismicity at Groningen gas field, the Netherlands: Post hoc evaluation and forecast update. Seismological Research Letters, 94, 1429–1446. https://doi.org/10.1785/0220220317

Erdogan, F. (1978). Mixed boundary-value problems in mechanics. In S. Nemat-Nasser (Ed.), *Mechanics today* (Vol. 4, pp. 1–86). Pergamon Press. https://doi.org/10.1016/b978-0-08-021792-5.50009-4

Erdogan, F., & Gupta, G. (1972). On the numerical solution of singular integral equations. *Quarterly of Applied Mathematics*, 29, 525–534. https://www.jstor.org/stable/45340623

Estrada, R., & Kanwal, R. (2000). Singular integral equations. Birkhäuser.

Fjaer, E., Holt, R., Horsrud, P., Raaen, A., & Risnes, R. (2021). Petroleum related rock mechanics, 3rd. Elsevier.

Garagash, D., & Germanovich, L. (2012). Nucleation and arrest of dynamic slip on a pressurized fault. *Journal of Geophysical Research*, 117(B10), B10310. https://doi.org/10.1029/2012JB009209

Geertsma, J. (1973). A basic theory of subsidence due to reservoir compaction: The homogeneous case. Verhandelingen Koninklijk Nederlandsch Geologisch Mijnbouwkundig Genootschap, 2S, 43–61.

Hills, D., Kelly, P., Dai, D., & Korsunsky, A. (1996). Solution of crack problems - The distributed dislocation technique. Kluwer Academic Publishers.

JANSEN AND MEULENBROEK 36 of 38



Journal of Geophysical Research: Solid Earth

- 10.1029/2025JB031577
- Hunfeld, L., Niemeyer, A., & Spiers, C. (2017). Frictional properties of simulated fault gouges from the seismogenic Groningen gas field under in situ P–T-chemical conditions. *Journal of Geophysical Research: Solid Earth*, 122(11), 8969–8989. https://doi.org/10.1002/2017JB014876
- Jansen, J., & Meulenbroek, B. (2022). Induced assismic slip and the onset of seismicity in displaced faults. Netherlands Journal of Geosciences, 101(e13), e13. https://doi.org/10.1017/njg.2022.9
- Jansen, J., & Meulenbroek, B. (2025). Matlab files used to produce the figures in the publication: The onset of depletion-induced seismicity in slip-weakening faults with interacting peaked shear stresses: Uenishi and Rice extended. (Version 1) [Software]. ResearchData, 4TU. https://doi.org/10.4121/2de552dc-108d-4446-9eb7-8b451e6ec072
- Jansen, J., Singhal, P., & Vossepoel, F. (2019). Insights from closed-form expressions for injection- and production-induced stresses in displaced faults. *Journal of Geophysical Research: Solid Earth*, 124(7), 7193–7212. https://doi.org/10.1029/2019JB017932
- Kalandiya, A. (1975). Mathematical methods of two-dimensional elasticity. Mir Publishers.
- Lehner, F. (2019). An analysis of depletion-induced fault stressing New closed-form analytical solutions (Tech. Rep). Nederlandse Aardolie Maatschappij. Retrieved from http://www.nam.nl/feiten-en-cijfers/onderzoeksrapporten.html
- Liu, D., Lecampion, B., & Garagash, D. (2019). Propagation of a fluid-driven fracture with fracture length dependent apparent toughness. Engineering Fracture Mechanics, 220, 106616. https://doi.org/10.1016/j.engfracmech.2019.106616
- Marelis, A., Beekman, F., & van Wees, J. (2024). 3D mechanical analysis of geothermal reservoir operations in faulted sedimentary aquifers using MACRIS. Geothermal Energy, 12(1), 5. https://doi.org/10.1186/s40517-024-00284-8
- Mason, J., & Handscomb, D. (2003). Chebyshev polynomials. Chapman & Hall.
- Meulenbroek, B., & Jansen, J. (2024). The use of Cauchy-type singular integrals over neighboring intervals to compute induced slip in displaced faults. *International Journal of Solids and Structures*, 300, 112922. https://doi.org/10.1016/j.ijsolstr.2024.112922
- Mulders, F. (2003). Modelling of stress development and fault slip in and around a producing gas reservoir (doctoral dissertation, Delft University of Technology). Retrieved from http://resolver.tudelft.nl/uuid:be742135-10d7-4d69-bdee-f808b5926065
- Multhopp, H. (1938). Die Berechnung der Auftriebsverteilung von Tragflügeln. Luftfahrtforschung, 15(4), 153-166.
- Muskhelishvili, N. (1953). Singular integral equations. Wolters-Noordhoff.
- Nagelhout, A., & Roest, J. (1997). Investigating fault slip in a model of an underground gas storage facility. *International Journal of Rock Mechanics and Mining Sciences*, 34(3–4), 212.e1–212.e14. https://doi.org/10.1016/S1365-1609(97)00051-8
- NAM. (2016). Winningsplan Groningen gasveld (Tech. Rep.). Nederlandse Aardolie Maatschappij (NAM). Retrieved from http://www.nam.nl/gas-en-oliewinning/groningen-gasveld/winningsplan-groningen-gasveld.html
- Novikov, A., Shokrollahzadeh Behbahani, S., Voskov, D., Hajibeygi, H., & Jansen, J. (2024). Benchmarking numerical simulation of induced fault slip with semi-analytical solutions. *Geomechanics and Geophysics for Geo-Energy and Geo-Resources*, 10(1), 182. https://doi.org/10.1007/s40948-024-00896-1
- Ohnaka, M. (2013). The physics of rock failure and earthquakes. Cambridge University Press.
- Orlic, B., & Wassing, B. (2013). A study of stress change and fault slip in producing gas reservoirs overlain by elastic and viscoelastic caprocks. Rock Mechanics and Rock Engineering, 46(3), 421–435. https://doi.org/10.1007/s00603-012-0347-6
- Pluymakers, A., Muntendam-Bos, A., & Niemeijer, A. (2023). Induced seismicity: A global phenomenon with special relevance to the Dutch subsurface. Netherlands Journal of Geosciences, 102, e2. https://doi.org/10.1017/njg.2023.2
- Rice, J. (1968). Mathematical analysis in the mathematics of fracture. In H. Liebowitz (Ed.), Fracture An advanced treatise (Vol. 2, pp. 191–311). Academic Press.
- Roest, J., & Kuilman, W. (1994). Geomechanical analysis of small earthquakes at the Eleveld gas reservoir. In SPE-ISRM rock mechanics in petroleum engineering conference. https://doi.org/10.2118/28097-MS (Paper SPE 28097. 29-31 Aug.,)
- Rudnicki, J. (2011). Eshelby's technique for analyzing inhomogeneities in geomechanics. In Y. Leroy & F. Lehner (Eds.), *Mechanics of crustal rocks* (pp. 43–72). Springer.
- Rutqvist, J., Rinaldi, A., Cappa, F., Jeanne, P., Mazzoldi, A., Urpi, L., et al. (2016). Fault activation and induced seismicity in geological carbon storage Lessons learned from recent modeling studies. *Journal of Rock Mechanics and Geotechnical Engineering*, 8(6), 789–804. https://doi.org/10.1016/j.jrmge.2016.09.001
- Scholz, C. (2019). In The mechanics of earthquakes and faulting, 3rd (ed.).
- Segall, P. (1989). Earthquakes triggered by fluid extraction. *Geology*, 17(10), 942–946. https://doi.org/10.1130/0091-7613(1989)017<0942: ETBFE>2.3.CO:2
- Segall, P. (2010). Earthquake and volcano deformation. Princeton University Press.
- Smith, J., Heimisson, E., Bourne, S., & Avouac, J. (2022). Stress-based forecasting of induced seismicity with instantaneous earthquake failure functions: Applications to the Groningen gas reservoir. Earth and Planetary Science Letters, 594, 117697. https://doi.org/10.1016/j.epsl.2022. 117697
- Uenishi, K., & Rice, J. (2003). Universal nucleation length for slip-weakening rupture instability under nonuniform loading. *Journal of Geophysical Research*, 108, 2042. https://doi.org/10.1029/2001JB001681
- Van den Bogert, P. (2015). Impact of various modelling options on the onset of fault slip and fault slip response using 2-dimensional finite-element modelling (Tech. Rep.). Shell Global Solutions International B.V. Retrieved from https://www.nam.nl/feiten-en-cijfers/onderzoeksrapporten. html
- Van den Bogert, P. (2018). Depletion-induced fault slip and seismic rupture: 2D geomechanical models for the Groningen field, the Netherlands (Tech. Rep.). Shell Global Solutions International B.V. Retrieved from https://www.nam.nl/feiten-en-cijfers/onderzoeksrapporten.html
- Van den Bogert, P., & Eijs, R. (2020). Why Mohr-circle analyses may underestimate the risk of fault reactivation in depleting reservoirs. International Journal of Rock Mechanics and Mining Sciences, 136(104502), 537–564. https://doi.org/10.1016/j.ijrmms.2020.104502
- Van den Hoek, P., & Poessé, J. (2021). Assessment of seismic risk in geothermal and hydrocarbon reservoirs using an exact analytical solution of stress change. In Proc. SPE europec featured at 82nd EAGE conference and exhibition. https://doi.org/10.2118/205122-MS
- Van Thienen-Visser, K., & Breunese, J. (2015). Induced seismicity of the Groningen gas field: History and recent developments. *The Leading Edge*, 34(6), 664–671. https://doi.org/10.1190/tle34060664.1
- Van Wees, J., Fokker, P., Van Thienen-Visser, K., Wassing, B., Osinga, S., Orlic, B., et al. (2017). Geomechanical models for induced seismicity in the Netherlands: Inferences from simplified analytical, finite element and rupture model approaches. *Netherlands Journal of Geosciences*, 96(5), S183–S202. https://doi.org/10.1017/njg.2017.38
- Van Wees, J., Pluymaekers, M., Osinga, S., Fokker, P., Van Thienen-Visser, K., Orlic, B., et al. (2019). 3-d mechanical analysis of complex reservoirs: A novel mesh-free approach. Geophysical Journal International, 219(2), 1118–1130. https://doi.org/10.1093/gji/ggz352
- Viesca, R., & Garagash, D. (2018). Numerical methods for coupled fracture problems. Journal of the Mechanics and Physics of Solids, 113, 13-34. https://doi.org/10.1016/j.jmps.2018.01.008
- Wang, H. (2000). Theory of linear poroelasticity with applications to geomechanics and hydrogeology. Princeton University Press.

JANSEN AND MEULENBROEK 37 of 38



Journal of Geophysical Research: Solid Earth

10.1029/2025JB031577

Weertman, J. (1996). Dislocation based fracture mechanics. World Scientific.

Wu, H., Rutqvist, J., & Vilarrasa, V. (2024). Analytical solution to quickly assess ground displacement for a pressurized or depleted deep reservoir intersected by a fault in a half space. *International Journal of Rock Mechanics and Mining Sciences*, 174, 105641. https://doi.org/10.1016/j.ijrmms.2024.105641

Wu, H., Vilarrasa, V., De Simone, S., Saaltink, M., & Parisio, F. (2021). Analytical solution to assess the induced seismicity potential of faults in pressurized and depleted reservoirs. *Journal of Geophysical Research: Solid Earth*, 126(1), e2020JB020436. https://doi.org/10.1029/2020JB020436

Zbinden, D., Pio Renaldi, A., Urpi, L., & Wiemer, S. (2017). On the physics-based processes behind production-induced seismicity in natural gas fields. *Journal of Geophysical Research: Solid Earth*, 122(5), 3792–3812. https://doi.org/10.1002/2017JB014003

JANSEN AND MEULENBROEK 38 of 38